Contents lists available at ScienceDirect

Journal of Materials Research and Technology

Microstructure evolution and deformation mechanisms of service-exposed P91 steel via interrupted uniaxial creep tests at 660 °C

R. Bonetti [a,*], N.C. Neate [b], A. Morris [c], P.H. Shipway [a], W. Sun [a]

[a] *Faculty of Engineering, University of Nottingham, Nottingham, NG7 2RD, UK*
[b] *Nanoscale and Microscale Research Centre, University of Nottingham, Nottingham, NG7 2RD, UK*
[c] *EDF Energy (UK), Coal and Gas Operations, Central Technical Organisation, Barnwood, Gloucester, GL4 3RS, UK*

ARTICLE INFO

ABSTRACT

Creep degradation behaviour of service-exposed P91 steel is evaluated during interrupted creep tests at 660 °C and 80 MPa using a number of material characterization techniques including transmission electron microscopy (TEM), scanning electron microscopy (SEM), electron backscattered diffraction (EBSD), energy dispersive spectroscopy (EDS) and optical microscopy (OM) to identify the microstructural evolution and the associated deformation mechanisms. Microhardness has also been measured in order to evaluate the softening mechanism. Under the creep conditions examined, microstructural degradation is found to be governed by the disappearance of the lath sub-structure, lath widening and recrystallization, as well as dislocation density reduction, coarsening of $M_{23}C_6$ and creep cavitation while MX and Laves phases are stable. Hardness evolution, extrapolated from hardness data obtained from uniaxial creep tests, is used to characterize the softening of the material. On this basis, hardness decrease is justified in term of the aforementioned microstructural changes. Implications of the findings for specific in-service life management in thermal plant piping systems are addressed.

Nomenclature

A	Parameter in Norton's law
b	Burgers vector
HV	Hardness at time t
HV_0	Hardness of the as-service-exposed material
n	Creep exponent in Norton's law
v	Average dislocation velocity
t	Time
t_r	Rupture time
$\dot{\varepsilon}$	Strain rate
$\dot{\varepsilon}_{ss}$	Minimum creep strain rate
σ	Stress
ρ	Dislocation density

1. Introduction

In the transition to a net zero carbon world, combined cycle gas fired (CCGT) thermal power stations will be essential to ensure enough on-demand generation is available and to meet the requirement for higher electricity demand [1–3]. The expansion of renewables generation will naturally, over time, lead to more intermittent operation of CCGT stations, which will place harsher demands on the integrity of their high temperature steam components and pipework systems that will be required to operate more flexibly [4,5]. In addition to this, newly constructed thermal power plants may be required to operate with carbon capture technology and operate at higher efficiency (up to 50%) in the ultrasupercritical regime or in advanced ultrasupercritical cycles at temperature of 700 °C and above, with pressure higher than 30 MPa in order to reduce CO_2 emissions [6–10]. Creep damage is one of the main causes of failure and concern for materials exposed to high temperature and pressure in modern power plants. A prolonged creep exposure is responsible for the deterioration of material properties so that methods to estimate and predict the remaining life of components are urgently needed [6,11,12]. One of the main factors responsible for the reduction of creep strength is the nucleation, growth and coalescence of cavities that is related to the microstructure evolution under high temperature service conditions and material composition, which causes a transition from a ductile to brittle fracture [13,14]. This study aims to improve the understanding of the microstructural evolution of P91 steels in service since this will become increasingly important for the operator in order to safely manage power generation systems and to remain commercially viable. In addition, a deep and clear knowledge of the microstructural changes will allow the development of modified and

more advanced versions of P91, which are crucial for the achievement of the new thermal efficiency target [15].

P91 steels, and more in general high strength 9–12% Cr steels are in widespread use in high temperature components (boiler headers, superheaters, reheaters) and pipework found in many modern power generation stations thanks to their superior qualities compared to more traditional materials (e.g. low alloy ferritic steels) [11]. 9–12%Cr steels show lower thermal expansion coefficient and higher thermal conductivity, improved corrosion and oxidation resistance, improved creep and fatigue properties [16,17]. These improved performances are achieved by a complex microstructure obtained after the carefully controlled heat treatments of quenching and tempering and by specific alloying elements in the chemical composition of the steel as Cr, Mo, V, Nb and N [18]. In the as-manufactured condition, P91 steel shows a tempered lath martensitic matrix with a hierarchical structure composed of prior austenitic grains (PAGs) containing inside lath blocks within packets characterized by a high dislocation density [19–22]. This already creep resistant microstructure is further strengthened by the precipitation of carbides and carbonitrides during tempering. The major precipitates are $M_{23}C_6$ carbides rich in Cr distributed along grain boundaries and MX carbonitrides predominantly rich in Nb and V found in the interior of the grains and to a lesser extent along grain boundaries [18,23,24].

Under long-term creep conditions, creep failure for P91 steel occurs primarily in the heat-affected zones (HAZs) of welds well before the estimated rupture life for the base metal due to Type IV creep cracking that originates from cavity nucleation and growth [10,25]. The base material also experiences a reduction of creep strength and failure before the predicted extrapolated life obtained from short-term creep life testing, due to void nucleation and inter-linkage [13]. To underpin the safe operation of components it is therefore of vital importance to understand the root causes of cavity formation in the microstructure and the impact of material composition on cavity nucleation. Common microstructural changes for P91 steel under service exposure that lead to cavity formation and final failure are recovery of the lath martensitic microstructure, precipitation and coarsening of Laves phase, coarsening and agglomeration of $M_{23}C_6$ and MX particles and formation of Z-phase [19,20,22,26,27].

Currently P91 systems are managed in a similar way to other high temperature steels in that confirmation of condition is ascertained during periodic invasive statutory physical inspections where non-destructive inspections and field metallographical inspections and assessments are undertaken. The application of non-destructive techniques (NDTs) has proven the most reliable method to determine the in-service condition [28]. An exhaustive review of NDTs normally used in power generation industry and in oil and gas plants is given by Sposito et al. in Ref. [29] and their use to assess creep damage is shown in Fig. 1.

Hardness measurement, among all NDTs, is routinely used in combination with metallographic replication during outage overhauls to provide an indication of creep softening over time and has been used predictively for the estimation of the remaining life in plant applications, often in conjunction with the Larson Miller parameter (LMP) [11, 30–32]. Hardness reduction is due to the primary material degradation processes listed above as precipitation coarsening and change in the lath structure thus allowing an estimation of the evolution of creep resistance and consequently of material life [33,34].

The challenges associated with evaluating the remaining life of in-service P91 steels using common field inspection techniques are well known and these can be summarized as, i) uncertainty in determining optimal and necessary locations for inspection, ii) defining the optimal time to perform inspections and to conduct preventive maintenance in order to ensure integrity of plant operations, iii) selection of the best combination of NDTs able to detect early stages of creep damage, iv) criticality of operations, skilled workforce and cost [28,35]. As a result of this, in practice the long-term creep life on operating power plants has invariably shown to be below the design life estimates extrapolated from short-term creep data, probably due to some differences in the metallurgical evolution [13,16,36,37].

The challenge for field examination is how to detect meaningful changes in microstructure or physical properties from periodic inspections and with sufficient time to implement practical mitigations, which could be repairs, replacements or adjustments to operating conditions to maintain continued safe operation. The final aim is therefore the development of an optimal and integrated creep monitoring strategy that allows a reliable assessment of the remaining life of components
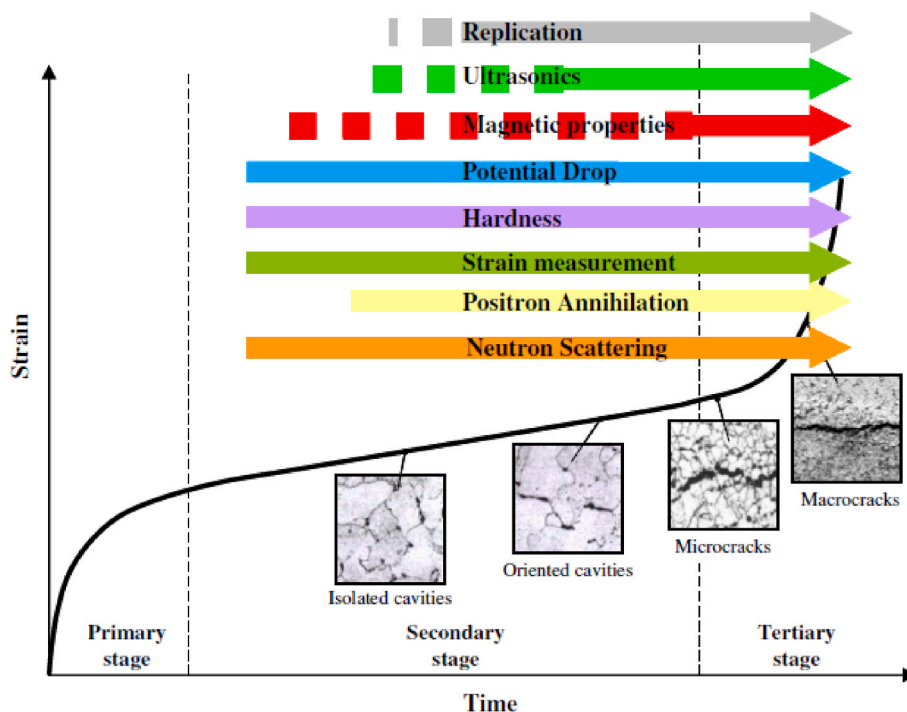

Fig. 1. Typical creep curve showing a typical evolution of creep damage with a qualitative overview of NDT and their range of applicability [29].

operating under creep. The opportunity is to consider, and if possible develop, improved assessment models that take account of the in-service ageing characteristics and therefore provide an earlier and more reliable remnant life assessment. This paper investigates some of the ageing characteristics that have potential to be used in creep lifing models, based on examination of interrupted uniaxial creep tests.

Interrupted creep tests have been extensively performed both under short-term and long-term creep conditions at different temperatures and stresses to study the microstructural mechanisms responsible for material degradation [23,30,38–40]. Short-term and long-term creep tests are in accord in the identification of primary processes that govern the microstructural evolution for 9–12% Cr steels, the key ones being the transformation of the original martensitic lath structure, reduction in dislocation density and coarsening of precipitates. Processes such as the precipitation of Z-phase and Laves phases are also observed under long-term creep exposure, but despite this, it has been argued that short-term creep tests are broadly sufficient in providing key information related to material degradation as a result of microstructural changes [38].

In this work, a series of interrupted creep tests at 660 °C and 80 MPa have been performed on a service-aged P91 steel removed from a superheater pipe. After each test, the microstructure evolution is studied using transmission electron microscopy (TEM), scanning electron microscopy (SEM), backscattered diffraction (EBSD), energy dispersive spectroscopy (EDS) and optical microscopy (OM). TEM is used primarily for imaging of dislocation arrangement, nano-scale precipitates and substructure detection. SEM has been employed for fracture surface analysis, and for imaging of the distribution of large scale precipitates and of high angle boundaries (prior austenitic grains, packets and blocks). EBSD has been employed for analysis of crystallographic orientation and phase detection. EDS has been employed for chemical analysis of the identified phases and optical microscope for cavities count. Vickers hardness has been measured with a microhardness test machine.

The main objective of the paper is the investigation of the microstructural evolution and the degradation mechanisms responsible for the reduction in creep strength and hardness leading to the final fracture. The understanding of creep damage, strengthening and degradation mechanisms is of primary importance for power industry operators in order to assess the reliability and safety of the components during operation to the end of service life. A well-organized microstructural evolution analysis allows the understanding of the effect of the microstructural evolution on the creep strength of the material. Indeed, the relationship between microstructural evolution and creep strength is still not well understood. In addition, the paper aims to clarify which microstructural factors are most influential for each creep stage. This is important because of the practical reliance on periodic physical inspections through life.

Even if creep damage is often concentrated in HAZ for P91-based structures, a comprehensive study on the behaviour of the base material after service exposure is still lacking and therefore required [13,41]. Finally, the importance to develop physics-based hardness models and how to use them in conjunction with other condition monitoring techniques for the purpose of life assessment will be discussed.

2. Material and experimental work

The P91 pipe material under investigation was provided by RWE Generation UK and removed from the HP Superheater Field Outlet tee manifold of a CCGT power station. The pipe operated under HP steam conditions which are 137 bar, 565 °C and, at the time of removal, the unit had run for 41,477 h with 1037 starts. The hoop stresses in the main steam pipework are estimated to vary between 63 and 77 MPa. The material is P91 EN10216-2, X10CrMoVNb9-1 with the compositional specification as detailed in Table 1.

Cr provides oxidation and corrosion resistance and allows the formation of $Cr_{23}C_6$. Mo is added to improve the creep strength under high temperature conditions via solid solution strengthening. V, Nb promote the formation of MX carbonitrides with the purpose to increase the creep resistance through precipitation strengthening. Si has been found to be useful for the improvement of oxidation resistance. The addition of Ni gives a better thermal resistance and, similarly to Cr, corrosion/oxidation resistance, improving at the same time the creep strength. Mn helps to stabilize the austenite phase [42–44]. The understanding of the significance of the chemical composition is extremely important as it affects the final microstructure and the creep properties of the material. The Electric Power Research Institute (EPRI) published a guideline for the specification of alloying elements in 9–12%Cr steels as some of the elements cause susceptibility to cavity formation and are related to a reduction in creep ductility [45].

2.1. Creep tests

Uniaxial cylindrical creep specimens were machined out from the received tee material with a gauge length of 50 mm and gauge diameter of 10 mm. The dimensions of the specimen are shown in Fig. 2.

All creep tests were performed in air in a creep testing machine equipped with a resistance furnace at 660 °C under a stress of 80 MPa, with the loading direction along the longitudinal axis of the specimen. The value of the applied stress was chosen to reflect the service hoop stress in the main steam pipework while the test temperature is higher than the operating temperature to reduce the test time. Three thermocouples positioned equally along the gauge length allowed to obtain a homogeneous temperature while a high-temperature extensometer was used to measure the creep strain.

A total of four creep tests were conducted and the corresponding creep strains with times are recorded in Table 2. A continuous creep test until failure (t_r) was first conducted, followed by interrupted creep tests at selected time ratio $t/t_r = 0.43, t/t_r = 0.9, t/t_r = 0.98$. For the complete test, the failure occurs at 3281 h. The interrupted creep tests have been selected intentionally in the secondary and tertiary creep stages to monitor and investigate the evolution of the main microstructural factors affecting the properties of the macrostructure.

Creep strain versus time and creep strain rate versus life fraction are reported in Fig. 3. The creep rate was calculated from raw creep data using the moving average function in Matlab over 60 neighbouring points.

2.2. Microstructural investigation techniques

After creep tests, the samples for microstructural investigation were obtained by cutting the specimen in the gauge region perpendicularly to the direction of loading application. Sections were taken close to the middle of the gauge section and specifically in regions where cracks had started to appear on the external surface in samples which had entered tertiary creep. After cutting and hot mounting in Bakelite resin, the sample cross-sections were ground with silicon carbide papers and polished with diamond paste, followed by colloidal silica. Etching with Villella's reagent was conducted only for samples used in SEM and

Table 1
Compositional specification of P91 steel.

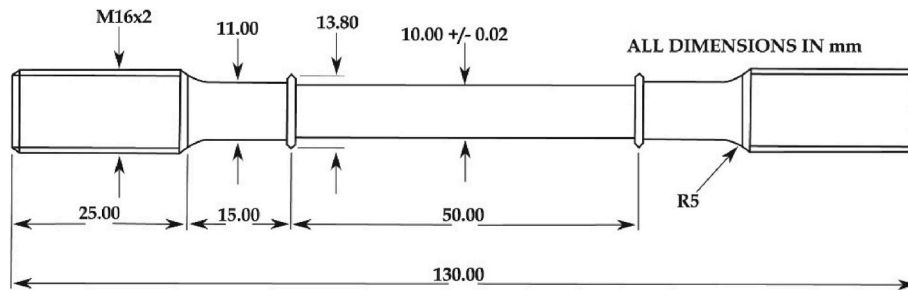| Element	C	Si	Mn	Ni	P	S	Cr	Mo	V	N	Nb	Al	Fe
min (wt%)	0.08	0.2	0.3				8	0.85	0.18	0.03	0.06		To balance
max (wt%)	0.12	0.5	0.6	0.4	0.025	0.015	9.5	1.05	0.25	0.07	0.1	0.03	

Fig. 2. Uniaxial creep test specimen [46].

Table 2
Creep strain and life fraction obtained from creep rupture and interrupted tests at 80 MPa and 660 °C.

Test Conditions	Creep Tests	Creep strain [%]	Time [hours]	t/t_r
σ = 80 MPa, T = 660 °C	1	2	1500	0.43
	2	4	2950	0.9
	3	7	3213	0.98
	4 (failure)	21.4	3281	1

optical microscope. The microstructure was studied with a range of techniques.

EBSD and EDS techniques were used to understand the changes in the crystallographic orientation of the sample and to characterize the variations within the crystal structure in terms of size and nature of phases. This was conducted with a JEOL JSM-7100F field emission gun SEM fitted with an Oxford Instruments AZtec EBSD and EDS system, using NordlysMax3 and X-Max 150 detectors. The following settings were used: SEM – accelerating voltage 15 kV, probe current 2–3 nA, working distance 16–17 mm, sample tilt 70°; EBSD – binning 4x4, exposure time 47–55 ms, gain 3 to 5, averaging 2 to 4 frames, static and auto background subtraction, Hough resolution 64, detecting band centres, 8 bands, refined accuracy indexing mode, TruPhase identification with reference EDS spectra; EDS – energy range 20 keV, 2048 channels, process time 4. For EBSD indexing the phase definitions were: from AZtec's HKL Phases database – Fe body-centered cubic (BCC) [47]; from the Inorganic Crystal Structure Database – $Cr_{23}C_6$ (ICSD-62667 [48]), Fe Mo Si (ICSD-53434 [49]), Nb N.58 (ICSD-40075 [50]). The cubic ferrite phase was used for indexing the tetragonal martensite matrix because the technique is insensitive to small changes in lattice parameter ratios.

The mapping was conducted at different scales: 400 μm square with a step size of 0.8 μm to reveal the texture and general microstructure, 100 μm square with a step size of 0.3 μm to assess grain boundary misorientation and reconstruct PAGs, and 20 μm square with a step size of 0.075 μm to show the details of the microstructure including precipitates.

The raw maps were processed using Oxford Instruments AZtec and AZtecCrystal software. In AZtec the Analyze Phases tool was used to generate typical spectra for each phase from the map data. The EBSD maps were processed with AZtecCrystal, using the Auto Clean-up routine to remove wild spikes and some zero solutions. Pole figures were generated for the matrix phase with a contouring half-width of 10° and equal area upper hemisphere projection. Texture component maps were generated for the matrix phase, yielding area fractions. Kernel average misorientation (KAM) maps were generated for the matrix phase with a 3x3 kernel and a maximum angle of 20°. This angle was chosen because it included over 99.95% of pixels in the map with the widest misorientation distribution. The 'Parent Grain' analysis tool was used for the reconstruction of PAGs from the child martensitic microstructure. A Kurdjumov-Sachs (K–S) parent-child orientation transformation has been selected since it is known to yield the best prediction of the crystallographic orientation between the austenite (parent) and the resulting martensite (child) phases [40,51]. Following the K–S distribution, the grain boundaries created during the transformation that have a misorientation angle <20° are defined as low-angle boundaries (LABs) with high-angle boundaries (HABs) being defined as having a misorientation angle >20° and showing a peak in the region 30–60°.

The as-service-exposed and fractured P91 samples were observed also using the FEI Quanta 600 SEM using secondary electrons (SE) and backscattered electrons (BSE) in order to investigate the distribution of large precipitates along the grain boundaries, to study the topography of the ruptured surface and the typology of cavitation damage. The SEM had a tungsten filament electron source and was operated at an accelerating voltage of 20 kV. For SE imaging, spot sizes of 4.0 and 4.5 were used, and working distances from 13 to 19 mm. For BSE, spot size 6.0 and working distance 9 mm were used.

For TEM, thin lamellae were extracted from the bulk material of each sample using a FEI Quanta 200 3D focussed ion beam (FIB) SEM. The samples were thinned to under 200 nm, and then polished with a 5 kV ion beam to reduce beam damage using a Zeiss Crossbeam 550 FIB-SEM. Imaging, diffraction and EDS mapping were carried out on a JEOL JEM-2100 Plus TEM at 200 kV, with Gatan OneView camera and Oxford Instruments EDS system. A double-tilt sample holder and 20 μm objective aperture were used to obtain two-beam {110} bright field (BF) images showing dislocations and other defects. These are marked with the diffraction vector **g** for the grain at the centre of the image. The thickness of the lamella at each location was calculated by the Kelly-Allen technique from the spacing of the fringes in the convergent beam electron diffraction (CBED) patterns which were collected at {221} and {200} Kikuchi bands using spot size 2 nm, alpha 3 and camera length 500 mm. The thickness measurements were used for the estimation of the dislocation density with the line intercept method. Scanning TEM (STEM) BF images were collected with a 50 μm condenser aperture, spot size 4 and camera length 800 mm, to observe the nanoscale precipitates which are not visible with the SEM. EDS maps were collected to identify the precipitate phases.

OM was used to show the distribution of cavities and the images captured from OM were used in ImageJ software to analyze and count cavity density. The microscope used is Nikon Eclipse LV100ND with a Nikon DS-Ri1 camera attached that uses a Nikon LV-NCNT 2 motorised magnifier. The software used to process the images is the NIkon NIS-Elements calibrated by laboratory technicians. The processing of images with NIS-Elements included adding a scale bar to have size information and adjusting the focus, brightness and contrast to achieve high-resolution imaging. The images captured with OM were then imported into ImageJ software where firstly the scale was set using the known distance from the scale bar of the OM in order to present measurement results in calibrated units. Then, the adjust threshold black and white function was used to have the features (cavities) displayed in black and the background in white, any white dots found in the middle of the cavities were filled with the fill holes step and finally the Analyze Particles tool was employed on the entire image to obtain information about the count, the area and the size of cavities.
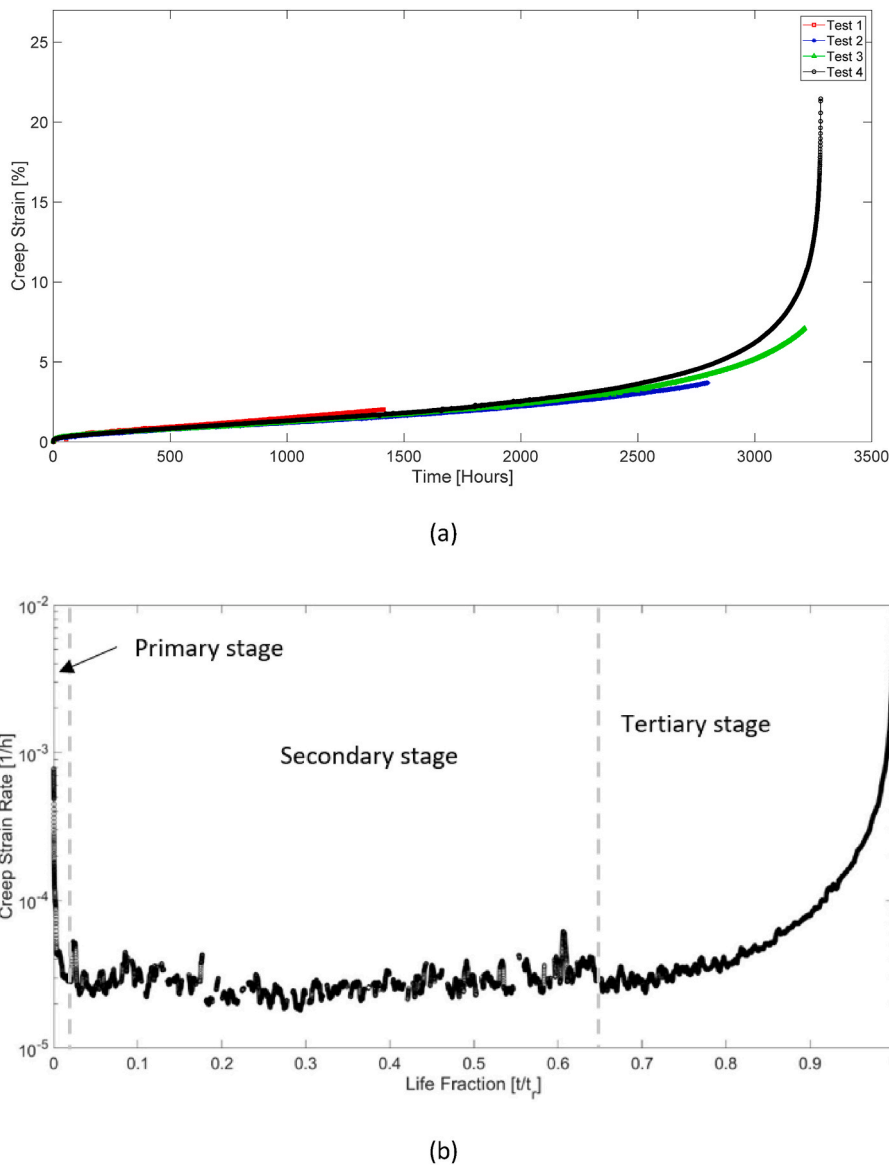
(a)

(b)

Fig. 3. Interrupted creep tests at 80 MPa and 660 °C, (a) Creep strain-time curves, and (b) creep strain rate-life fraction curves for Test 4 (test to failure)

Vickers microhardness testing was employed to measure the hardness of each P91 sample using a load of 1 kgf applied for 10 s. For every sample, the measurement was repeated 10 times at different locations to reduce the observational error. The microhardness tester used was a Buehler 1600 series set at 220 V AC. Hardness represents a practical method for investigating the softening mechanisms of the material as will be discussed later.

3. Results and discussion

3.1. Creep properties and mechanism

From the creep strain curves in Fig. 3a and the associated creep strain rates in Fig. 3b, it is noted that the primary creep stage is essentially negligible, while the secondary (steady-state) stage accounts for the largest portion of the specimen life (about 80%) before entering the tertiary stage with a rapid increase in creep rate and deformation until the final fracture. Since the temperature and the stress of the creep tests are kept constant, the variation in creep rate before the formation of necking is the result of changes in the internal structure of the material that occur due to creep strain and time at temperature.

Creep material properties can be deduced from the creep test curves. The value of the steady-state creep rate $\dot{\varepsilon}_{ss}$ and the value of the stress exponent n, obtained from the logarithmic form of the Norton's law (Equation (1)) once the creep constant A is known, are reported in Table 3.

$$\dot{\varepsilon}_{ss} = A \, \sigma^n \qquad (1)$$

The value of A is taken from Ref. [52] and the value of the shear modulus G is obtained from the relationship $G = E/2*(1 + \upsilon)$ where the Young's modulus $E = 218$ GPa at room temperature (RT), typical for P91 [53], and the Poisson's ratio $\upsilon = 0.3$ [54].

The calculated parameters σ/G and n suggest that the main creep deformation mechanism operating is dislocation (power-law) creep [55]. Dislocation creep is a result of the climb of dislocations that

Table 3
Creep properties associated with the creep curve (stress in MPa and time in hour).

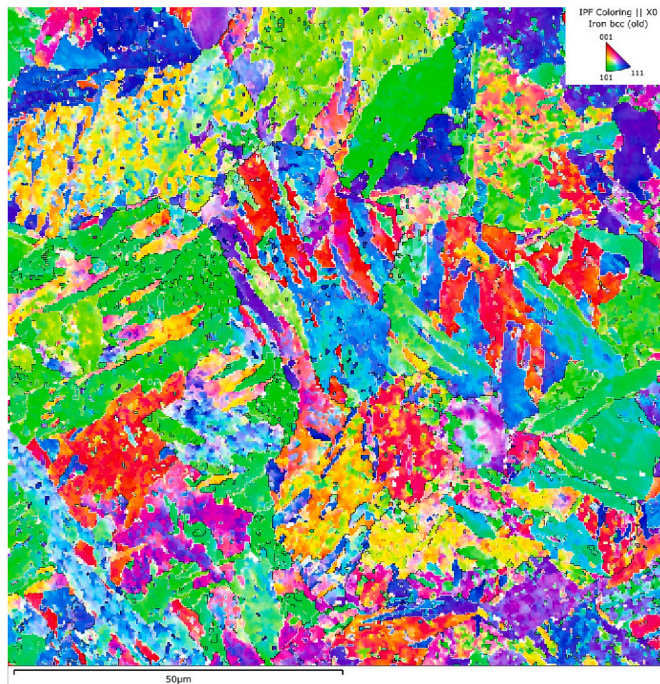| $\dot{\varepsilon}_{ss}\ [h^{-1}]$	A	G [GPa]	σ/G	n
1.1×10^{-5}	2.004×10^{-20}	83.85	0.95×10^{-3}	7.7

overcome obstacles aided by thermally activated mechanisms involving the diffusion of vacancies or interstitials [6,56,57].

3.2. As-service-exposed P91 material

The SEM SE image in Fig. 4a shows that the as-service-exposed material has the complex hierarchical structure typical for P91
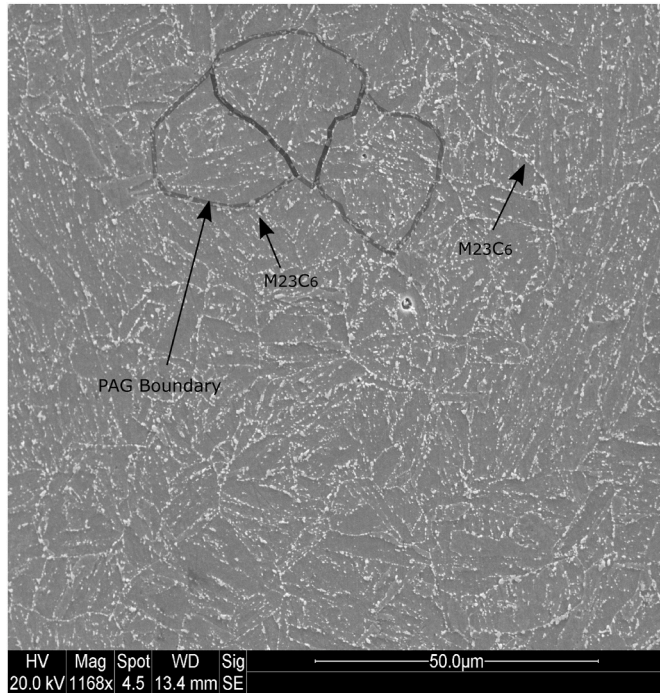
(a)

(b)

Fig. 4. Micrographs of as-service-exposed P91 material (a) SEM SE showing PAGs studded with $M_{23}C_6$ particles at grain boundaries, and (b) EBSD overview map with visible PAG boundaries in the range of 30–50° misorientation angles

composed of martensitic laths of the same crystallographic orientation contained inside blocks. The blocks are in turn contained inside packets. Different packets form the PAG from which the martensite originates after quenching. The average PAG size is 22 μm and the lath width in the as-service-exposed condition is 0.75 μm, values consistent with a typical P91 steel [40,58,59]. The martensitic matrix was indexed as ferrite (BCC) in the EBSD maps due to the technique being insensitive to small changes in the c/a ratio. LABs surround laths and sub-grains with misorientation angles <20° while blocks, packets and PAGs are enclosed in HABs [60,61]. The average misorientation angles for PAGs are in the range of 30–50° for the as-service-exposed material (Fig. 4b).

The TEM analysis reveals stable sub-grain structures in the laths as shown by the dotted lines in Fig. 5a. This suggests that the material under service conditions at high temperature is in a static recovery form in which the mobile dislocations inside the laths have moved along activated slip planes overcoming obstacles by thermal activation and by thermally assisted mechanisms such as vacancy diffusion [62]. As a consequence, the re-arrangement of mobile dislocations occurs and a well-developed sub-grain structure has developed in order to minimize the high elastic energy stored in the microstructure [63,64]. The sub-grain boundaries are therefore formed by a wall of dislocations that hinder the movement of the other free dislocations contained inside the laths, significantly increasing the creep resistance [65,66]. The as-manufactured P91 steel after the typical heat treatments of normalizing and tempering shows a lath martensitic structure which contains a large number of dislocations but sub-grains are not expected to form [67,68]. The formation of sub-grains within the laths occurs during the exposure to creep and add further strengthening to the material [46].

The static recovery condition can explain why the creep tests of the service-exposed material exhibit a negligible primary creep stage since recovery is a process that characterizes the secondary creep stage [55]. Dislocation density in the lath interior in the as-service-exposed state is high as visible in Fig. 5b and dislocation tangles are observed. The initial dislocation density has been calculated as being $1.6 \times 10^{14} \, \text{m}^{-2}$ using the line intercept method [66]. This value is approximately three times lower than that of as-received P91 material reported in Ref. [23] and in Ref. [69] and this is attributed to static recovery [23].

In terms of precipitates, the as-service-exposed sample has been found to be characterized by a fine distribution of $M_{23}C_6$ carbides, where M is predominately rich in Cr with traces of Fe and Mo (Figs. 5 and 6), along with nano-scale Nb/V-rich MX carbonitrides that are best detected using TEM due to their small size (Fig. 5a/b). M23C6 are located along LABs and HABs while MX are found to be distributed inside the laths in the sub-grain structure and in a lower measure along LABs. MX particles are pinning sites for the mobile dislocations as can be seen in Fig. 5b, strongly increasing the creep strength of P91 via precipitation strengthening [21,41]. Also, $M_{23}C_6$ and MX that are spread along grain boundaries (GBs) stabilize the microstructure, retarding the migration of the GBs under service conditions, and thus highly increasing the resistance to static recrystallization and grain growth (Fig. 5c/d) [24].

MX carbonitrides and $M_{23}C_6$ carbides precipitate out in the initial martensitic microstructure from the supersaturated solid solution after quenching and tempering heat treatments. As reported from previous studies, $M_{23}C_6$ carbides nucleate copiously along GBs favoured by the misorientiation between adjacent grains and the orientation of the GB [70,71]. The $M_{23}C_6$ precipitates have a specific crystallographic orientation relationship indicating a coherent interface with at least one of the adjoining grains for which the boundary plane is close to the plane of the precipitate [72,73]. MX carbonitrides precipitate mainly in the interior of the martensitic laths thanks to the coherency between their lattice and the surrounding ferritic matrix [21].

(Fe,Si)$_2$Mo-type Laves phase enriched in Fe, Mo and Si, with an average initial size of 300 nm is also identified mostly along PAG boundaries and partially on lath boundaries (Fig. 5a, white arrows for Laves phase). (Fe,Si)$_2$Mo-type Laves phase is formed and results in depletion of Mo in the matrix, causing a reduction of solid solution
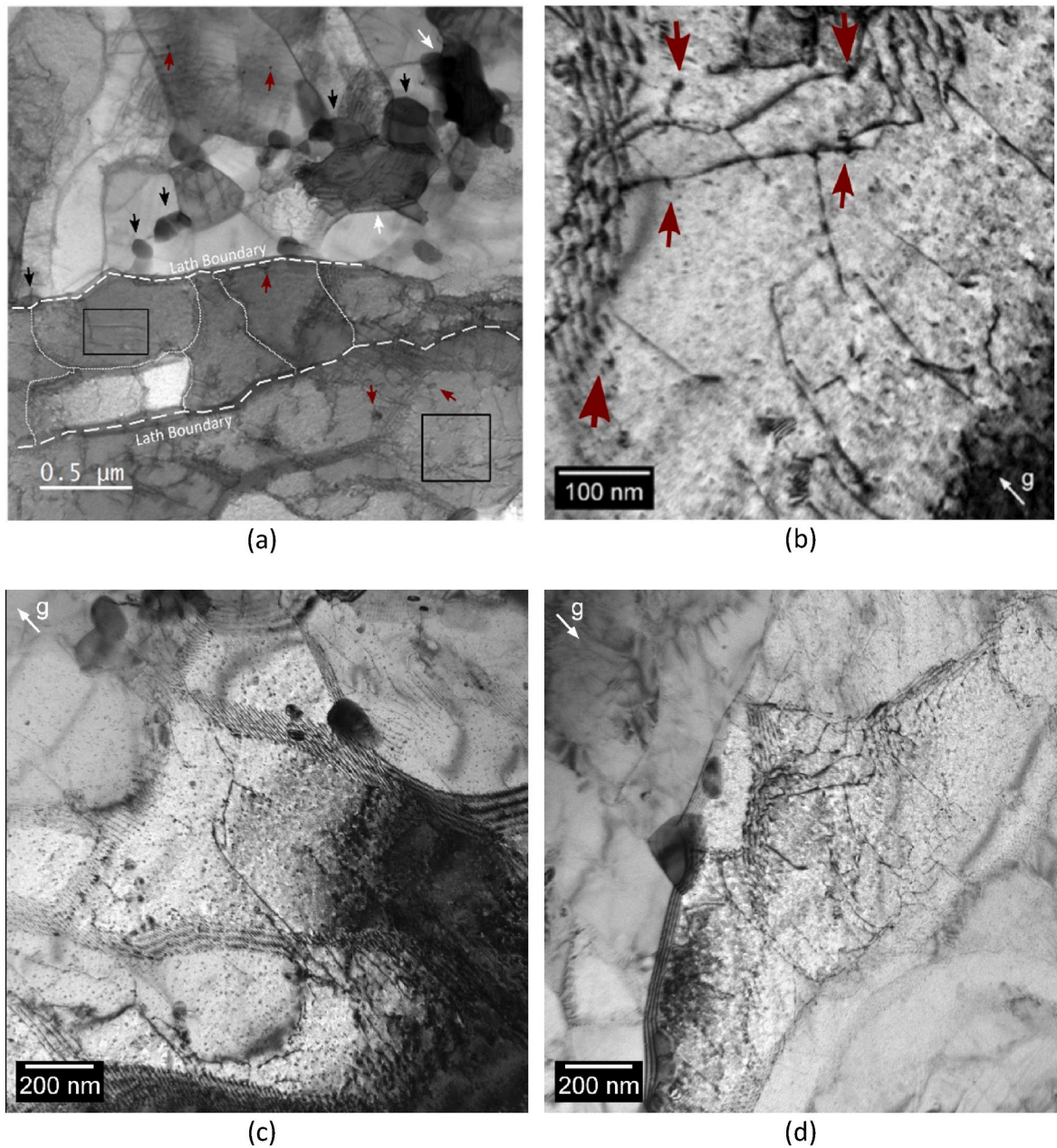
Fig. 5. (a) STEM BF image of the as-service-exposed P91 material showing lath and sub-grain boundaries (dotted lines) and precipitates identified from EDS maps (red arrows for MX, black arrows for $M_{23}C_6$, white arrows for Laves phase), with square boxes to identify mobile dislocation inside the sub-grains. (b, c, d) Two-beam BF TEM images showing (b) line dislocations pinned by MX, (c) stabilization of sub-grains by MX and $M_{23}C_6$, and (d) $M_{23}C_6$ stabilizing effect on lath structure. (For interpretation of the references to colour in this figure legend, the reader is referred to the Web version of this article.)

hardening during service conditions [37]. Other studies report that the precipitation of Laves phase is beneficial for the strengthening of the material, at least in the early stage of creep deformation. Laves phase has a similar effect to $M_{23}C_6$, which increases the creep strength of the material by hindering grain boundary migration, thus retarding the growth of sub-grains [19,20,74]. The nucleation of Laves phase is accelerated by the presence of Si with Laves particles being found to form mostly in the proximity of $M_{23}C_6$ [75]. Two main mechanisms contribute to the nucleation of Laves phase. On one side, Si and Mo have a tendency to segregate to GBs and when the saturation of these elements is reached, Laves phase appears. On the other hand, $M_{23}C_6$ located along GBs act as preferential nucleation sites for Laves phase [20,42,75]. In virgin as-manufactured P91 steel, Laves phase is not observed, but it tends to precipitate after long-term creep with creep lives of around 1500 h at temperature higher than 600 °C [20,68].

The compositional makeup of the different precipitates is reported in Fig. 7. It is likely that the spectra for the precipitate phases include a contribution from the surrounding matrix, so quantification of the concentrations is not appropriate. However, the differences between these spectra and the matrix spectrum indicate which elements are present in the precipitates.

Summarizing, the creep strength in P91 alloys is achieved by the following microstructural strengthening mechanisms, all of which are still operative in the as-service-exposed alloy.

- Lath and sub-block martensitic structure;
- Finely distributed MX and $M_{23}C_6$ boundary precipitates that block the grains from migrating by pinning them;
- $M_{23}C_6$ boundary precipitates impede knitting reactions between free dislocations and sub-grains dislocations;
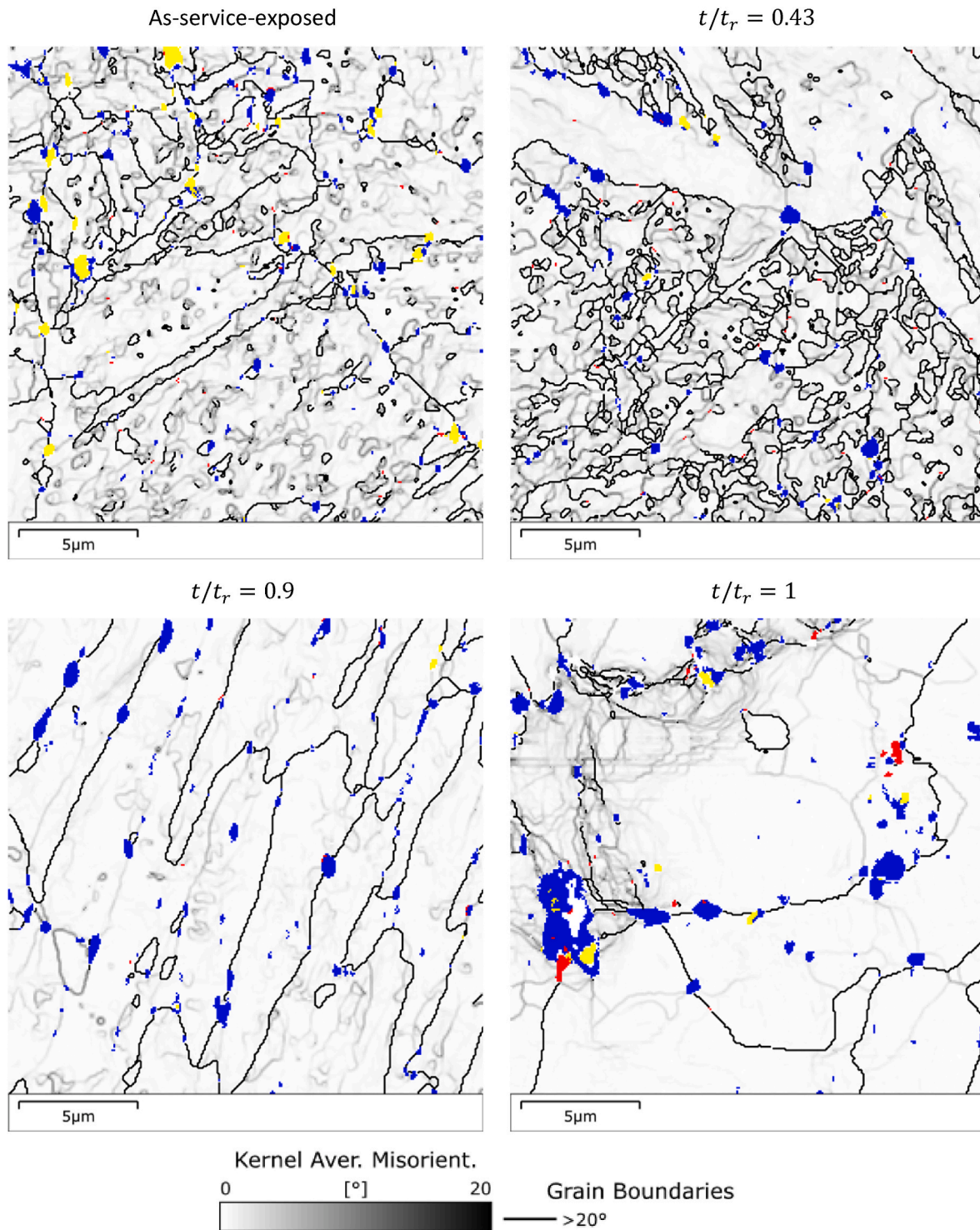
Fig. 6. Layered EBSD images with kernel average misorientation colouring and grain boundary lines for the matrix, and phase colouring for secondary phases, showing the distribution and evolution of $M_{23}C_6$ (blue), MX (red) and Laves phase (yellow). (For interpretation of the references to colour in this figure legend, the reader is referred to the Web version of this article.)

- Finely distributed MX in the ferritic matrix that obstruct the movement of mobile dislocations;
- Substitutional solid-solution by Mo in the matrix that impedes dislocation climb and glide.

3.3. Microstructure evolution under post-service (laboratory) creep deformation

To study the relationship between the post-service (laboratory) creep deformation and the related microstructural evolution of P91, a series of EBSD maps have been collected and processed to show misorientation angle (MA) and inverse pole figure (IPF) colouring, with corresponding pole figures (PF). TEM images were also captured for the interrupted and
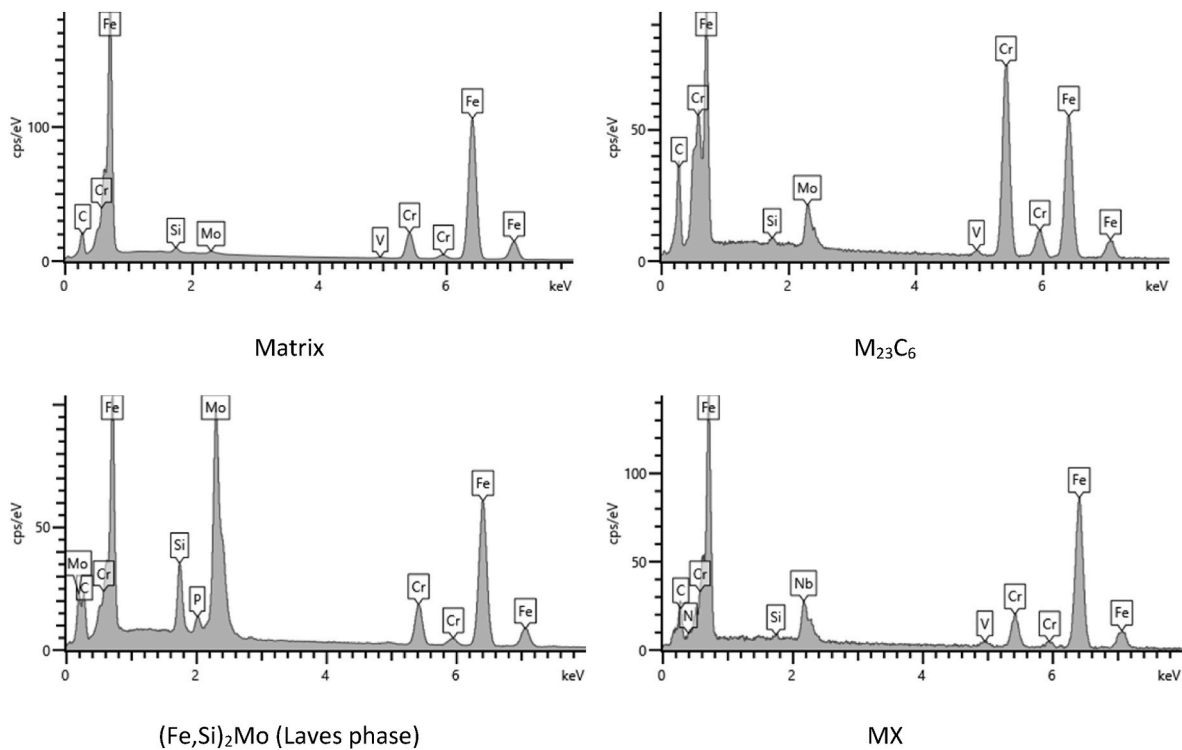
Fig. 7. SEM-EDS analysis of the composition of the four main phases observed in the maps in Fig. 6. The matrix (Iron based), $M_{23}C_6$, $(Fe,Si)_2Mo$ (Laves phase) and MX

test-to-failure laboratory creep tests. As noted previously, regions of the creep specimens investigated are perpendicular to the loading direction during the creep tests and chosen in the proximity of the highest strained area or where a crack was visible.

3.3.1. Disappearance of sub-grains, lath widening and formation of new grain structures

The results from EBSD mapping are shown in Figs. 8 and 9. The results for the failed specimen refer to the bulk material ~10 mm away from the fractured surface.
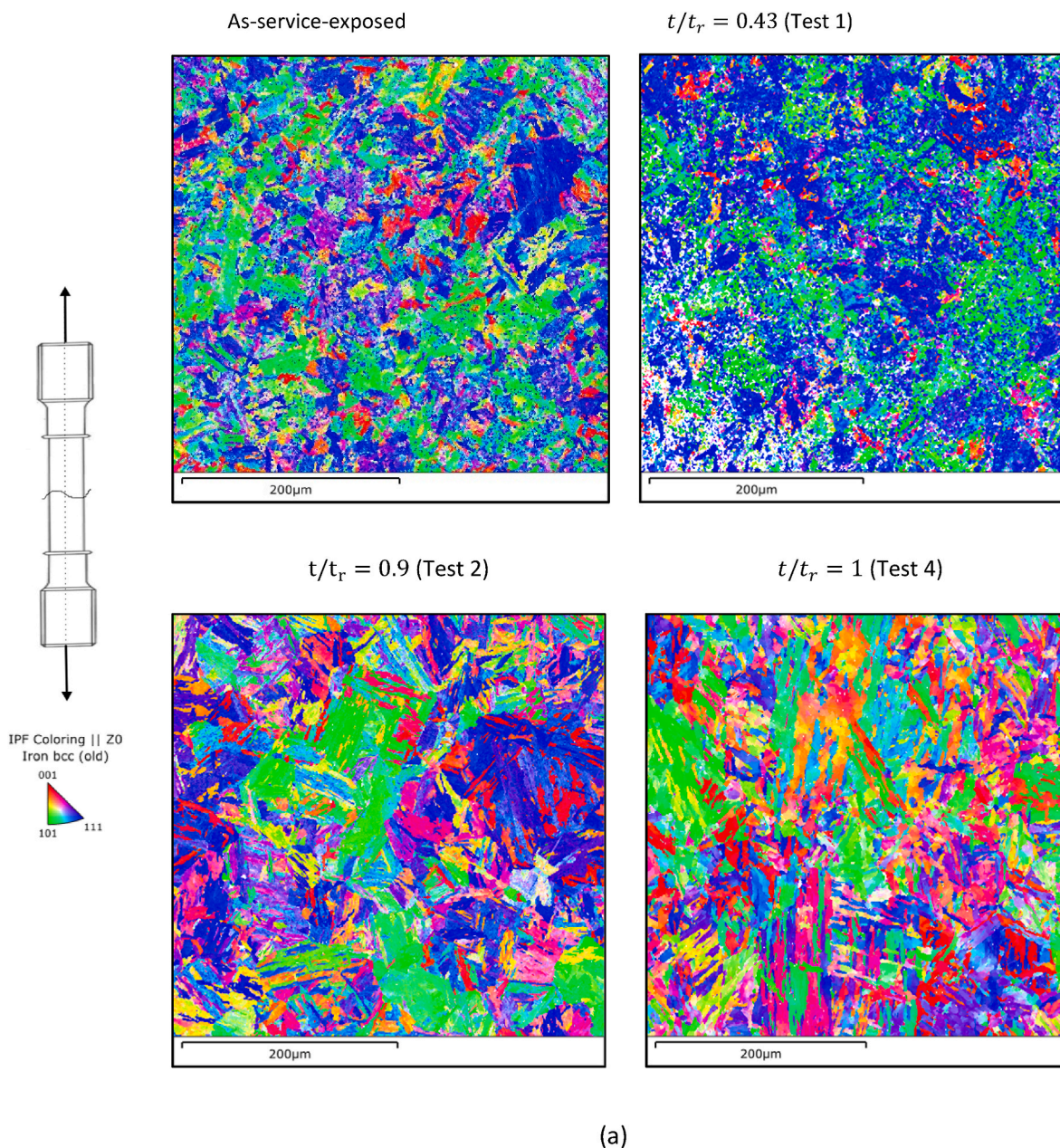
The IPF map for the as-service-exposed material has a high proportion of blue colouring (Fig. 8a), indicating that the $\langle 1\,1\,1 \rangle$ direction of the matrix crystal structure is frequently orientated parallel to the Z-direction (the axis of loading) of the sample. The PF in Fig. 8b reveals that this is a fibre texture with the $\langle 1\,1\,1 \rangle$ direction aligned to the Z-axis of the sample, which must be due to the original manufacture of the component. In Test 1 at $t/t_r = 0.43$ (secondary creep stage), there is a substantial strengthening of this texture, as shown by the increase in $\langle 1\,1\,1 \rangle$ pole density on the Z-axis in the PFs (from 5.2 times uniform density to 11.1 times). At the onset of the tertiary creep stage (Test 2 at $t/t_r = 0.9$) and continuing until failure (Test 4), the IPF-Z maps are less dominated by blue colouring, meaning that a change in the crystallographic orientation of the material has happened. The EBSD images in Fig. 6 also highlight an evolution of the microstructure from typical lath martensite until $t/t_r = 0.9$ (Test 2) to the appearance of new more equiaxed grains at fracture (Test 4).

In the corresponding PFs there is a reduction of the concentric pattern associated with fibre texture, and at failure it has disappeared altogether, leaving what appears to be a random distribution of orientations.

The strength of the fibre texture is quantified in terms of map area fraction in Table 4. The fraction corresponding to the texture increases by a multiple of 1.8 from the as-service-exposed specimen to $t/t_r = 0.43$, then reduces to below the initial value at $t/t_r = 0.9$, and reaches a value close to random orientation by failure.

In terms of grain boundary misorientations, there is a decrease of misorientation between 2° and 20° during creep deformation as underlined by KAM maps in Fig. 9 where the blue colouring on the map increases. Although the individual boundaries are not well resolved at this scale, the maps in Fig. 6 (at 0.075 μm step size) show that this range of misorientation is chiefly due to LABs. This suggests a strong reduction in the density of LABs from Test 1 ($t/t_r = 0.43$) to Test 2 ($t/t_r = 0.9$), and in Test 4 they are almost entirely absent. This means that at tertiary creep stage, the sub-grain structure has disappeared and is replaced by a new microstructure.

To further investigate the evolution of sub-grains and laths and to confirm the outcomes from EBSD mapping, TEM analysis has been performed (Fig. 10). The P91 steel following Test 1 creep ($t/t_r = 0.43$) still exhibits a sub-grain and lath structure not very different from the as-service-exposed state but where the lath width (Table 5) is slightly larger (Fig. 10a). Following Test 2 ($t/t_r = 0.9$), rapid microstructural changes happen that cause the creep rate to increase after reaching its minimal value. At Test 2, the sub-grain structure is broken with MX carbonitrides losing their capability of pinning sub-grain boundaries. Sub-grains have almost disappeared while laths are still present but are wider compared to the material following Test 1. The lath width in the materials from Test 2 is on average 1.3 μm (Fig. 10b). Progressing to Test 3 ($t/t_r = 0.98$), a new microstructure composed of equiaxed grain structures is observed while the laths have now disappeared (Fig. 10c). As the creep test progresses until creep failure (Test 4), the original martensitic structure is completely transformed into the newly microstructure with equiaxed grains (Fig. 10d) [42]. This new microstructure is very similar to a typical hot-deformed structure suggesting that some form of dynamic recrystallization has taken place as the material approached failure after the occurrence of necking. The neck region is characterized by a local increase in creep rate due to a higher local stress that favour the transition to this type of microstructure [24,37]. This is an interesting phenomenon already known for other high stacking fault energy materials such as martensitic stainless steel [76] but it is still not well understood for P91 steel, which will require further investigation [77].

As-service-exposed $t/t_r = 0.43$ (Test 1)

$t/t_r = 0.9$ (Test 2) $t/t_r = 1$ (Test 4)

IPF Coloring || Z0
Iron bcc (old)
001
101   111

(a)

Fig. 8. (a) IPF-Z maps and (b) Contoured PFs (upper hemisphere, equal area projection) for the matrix phase for the as-service-exposed P91 and for the same material after three subsequent creep test exposures as indicated.

Regardless, the equiaxed grain structure is not supposed to significantly influence the lifetime of the material since it is developed at the end of the tertiary creep stage just before failure when gross changes in microstructure have already taken place [37].

The presence in the matrix of these equiaxed sub-grains after creep is also revealed and confirmed by SEM-BSE investigations (Fig. 11). This finding is consistent with results presented by Panait et al. [37]. Fig. 11 shows also the distribution of Mo-rich Laves phase particles after creep being identified as the bright particles in BSE imaging.

3.3.2. Dislocation density variation

The vanishing of LABs, the disappearance of sub-grains and the coarsening of the lath structure is explained by the annihilation theory developed by Fournier et al. [58] and Sauzay [78]. Under creep conditions, mobile dislocations climb and glide along specific activated slip systems (according to the dislocation creep mechanism, see Paragraph 3.1) and interact with the boundary dislocations that form the sub-grain structure. When these two types of dislocations have an opposite sign, they annihilate each other. Also, mutual annihilation can occur in the case of two mobile dislocations that eliminate each other because of opposite sign [79,80]. As a consequence, the dislocation density decreases accompanied by the disappearance of the sub-structure and the widening of lath structures [59]. This annihilation process is called dynamic recovery [69]. The variation of dislocation density is reported in Table 5.

The rapid decrease of mobile dislocations between the as-service-exposed state and following Test 1 (so during an early stage of creep deformation) is due to the dynamic recovery mechanism [39]. This high annihilation rate of mobile dislocations at the beginning of creep has also been stated in other experimental observations [37,74].
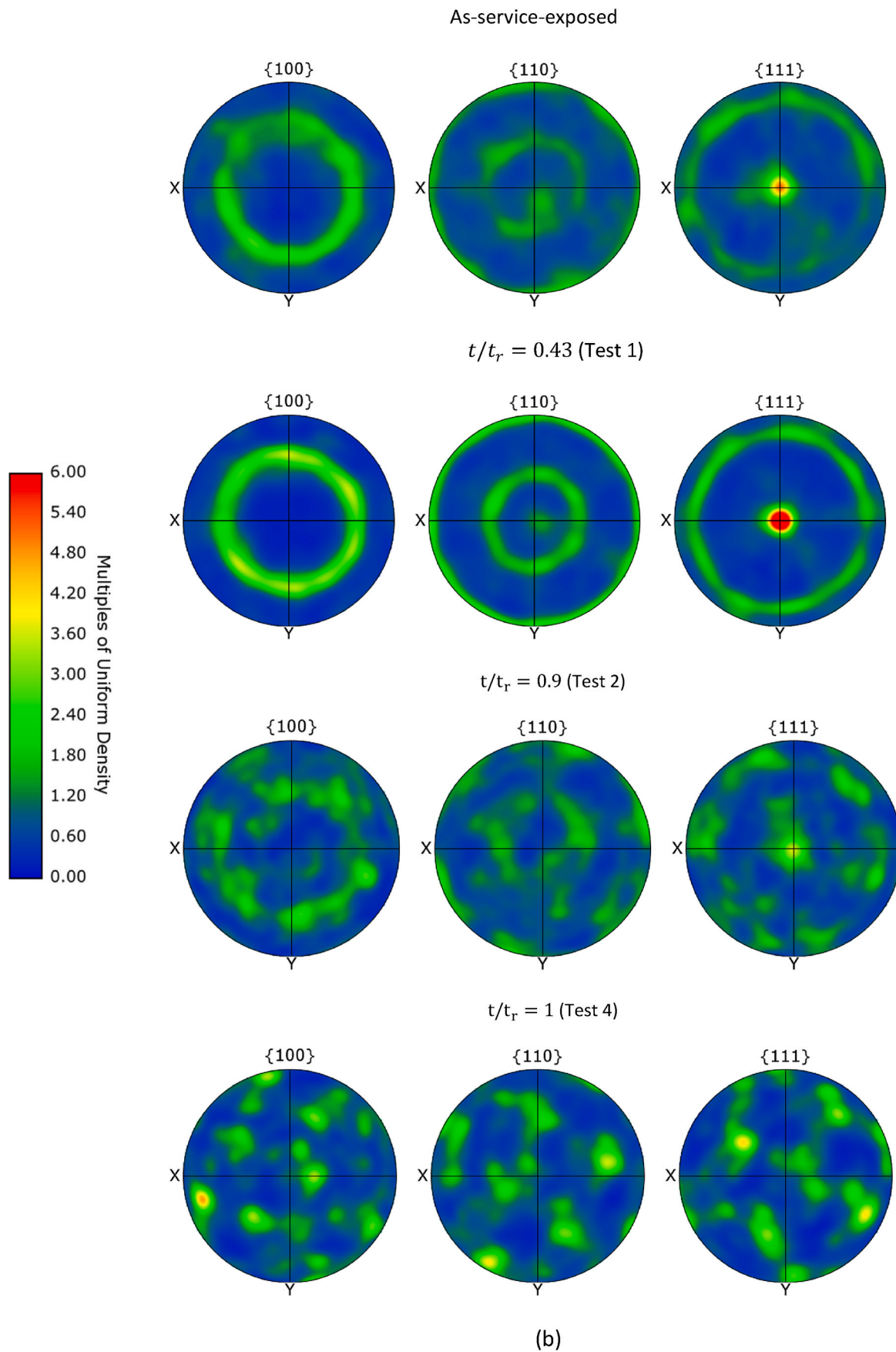
As–service-exposed

$t/t_r = 0.43$ (Test 1)

$t/t_r = 0.9$ (Test 2)
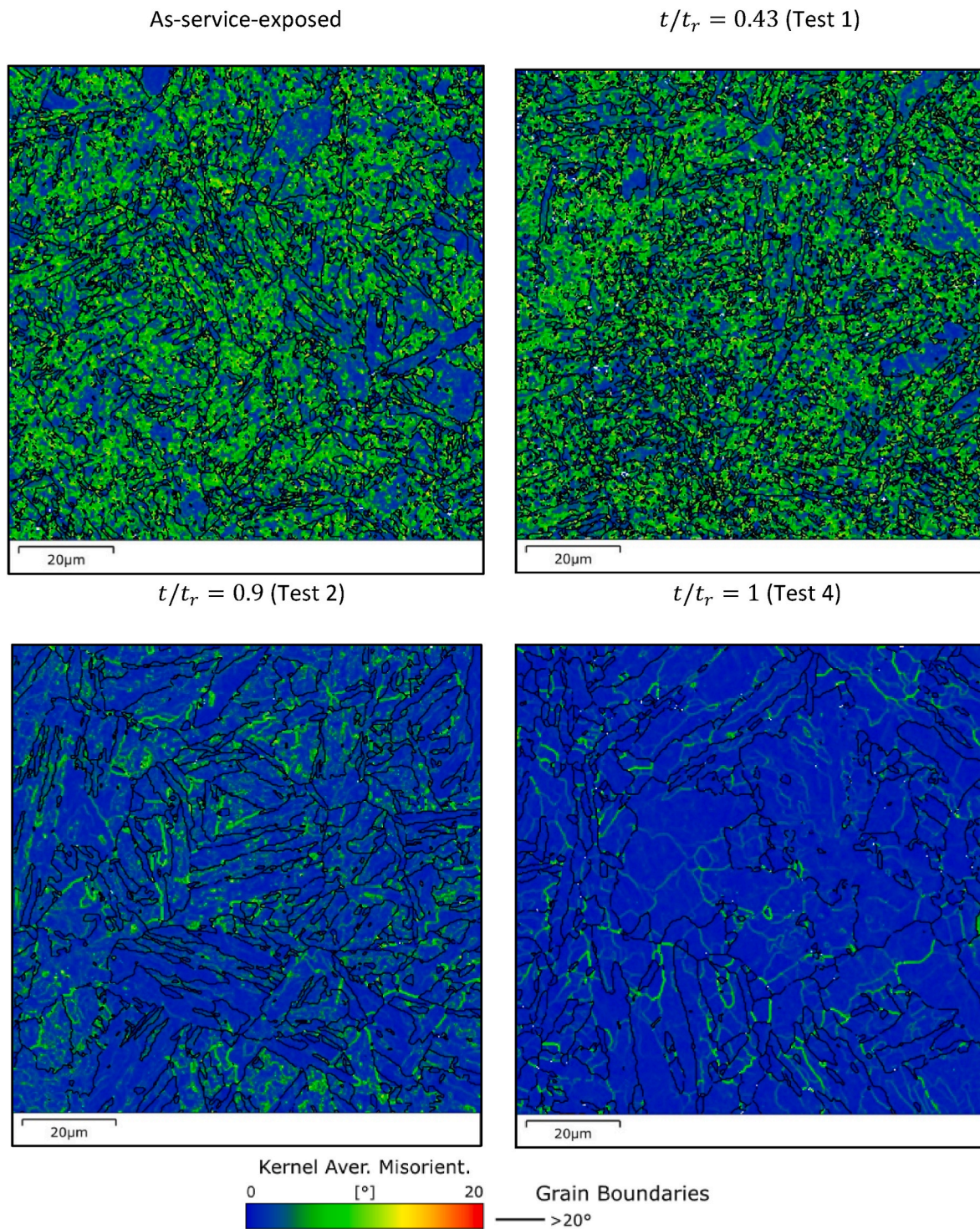
$t/t_r = 1$ (Test 4)

(b)

Fig. 8. (*continued*).

Fig. 9. KAM maps for the as-service-exposed P91 and for the same material after three subsequent creep test exposures as indicated. See Fig. 6 for more detailed misorientation maps.

Table 4
Area fractions of the maps in Fig. 7 that are within $10°$ of the fibre texture $\langle 1\,1\,1 \rangle \parallel$ Z.

t/t_r	Area fraction (%)
As-service-exposed	23.3
0.43	41.8
0.9	17.3
1	5.3
Random orientation	6.1

Mobile dislocations are responsible for creep deformation. The relation between creep and dislocation density is governed by the Orowan equation reported below:

$$\dot{\varepsilon} = \rho\, b\, v \tag{2}$$

where $\dot{\varepsilon}$ is the creep strain rate, ρ is the density of mobile dislocations, b is the Burgers vector, v is the average dislocation velocity. Creep strain acceleration is related to subgrain coarsening due to dynamic recovery causing as consequence the decrease of material hardness under creep
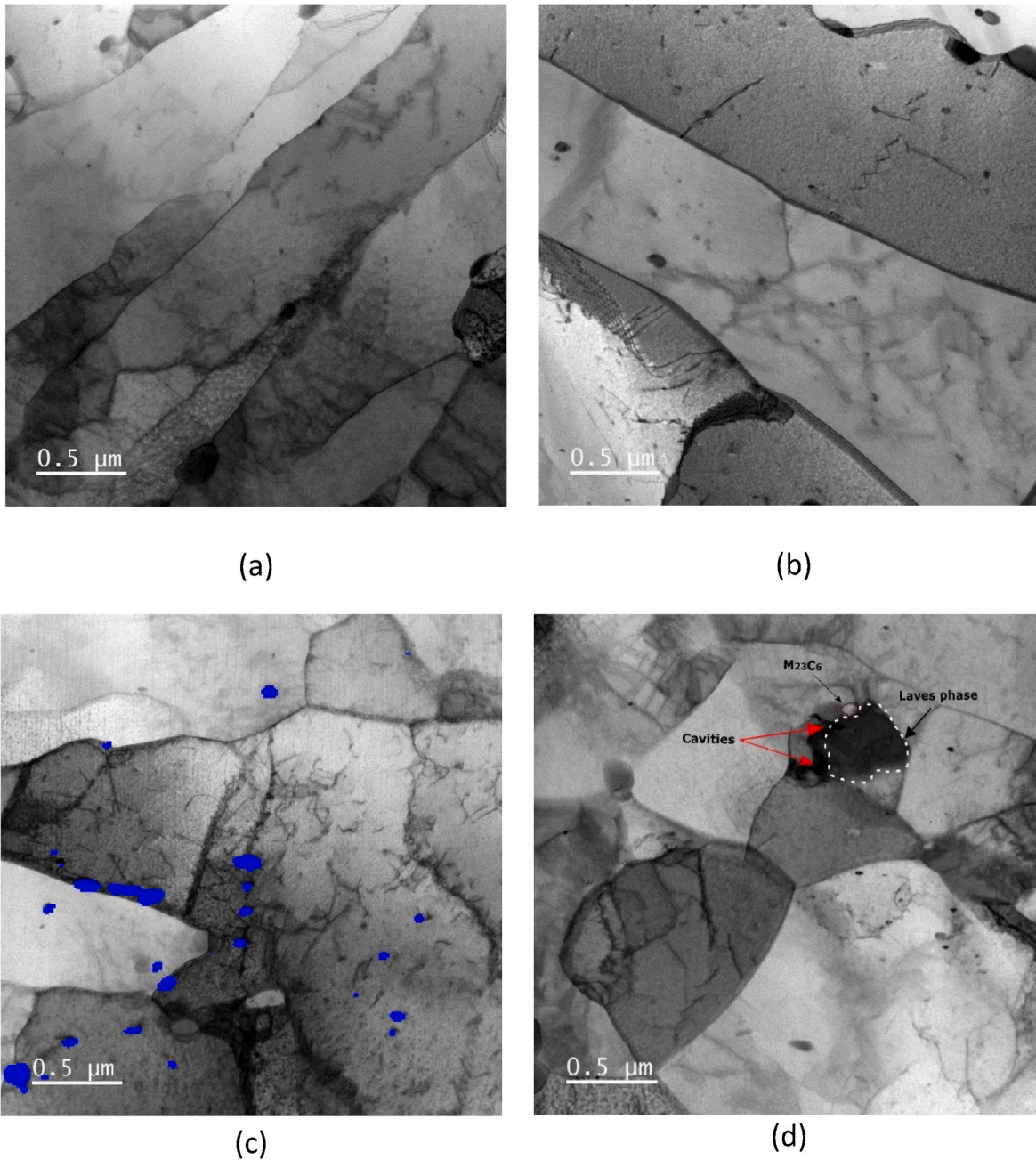
Fig. 10. BF STEM micrographs (camera length 800 mm) showing the evolution of as-service-aged P91 microstructure following creep (a) Test 1 $t/t_r = 0.43$, (b) Test 2 $t/t_r = 0.9$ with visible MX inside the lath, (c) Test 3 $t/t_r = 0.98$ showing the formation of equiaxed grains (blue spots for V-rich MX), and (d) Test 4 $t/t_r = 1$ showing the complete transformation to an equiaxed grain structure. (For interpretation of the references to colour in this figure legend, the reader is referred to the Web version of this article.)

Table 5
Density of mobile dislocation evolution, size of $M_{23}C_6$ precipitates, lath width and cavity density.

	As-service-exposed	$t/t_r = 0.43$	$t/t_r = 0.9$	$t/t_r = 0.98$	$t/t_r = 1$
Dislocation density [x10^{13}m^{-2}]	16	6.5	5.8	4.9	2.6
$M_{23}C_6$ [nm]	120	140	154	198	250
Lath width [µm]	0.75	0.89	1.3		
Cavities [cavities/mm^2]	565	745	1300	2400	2800

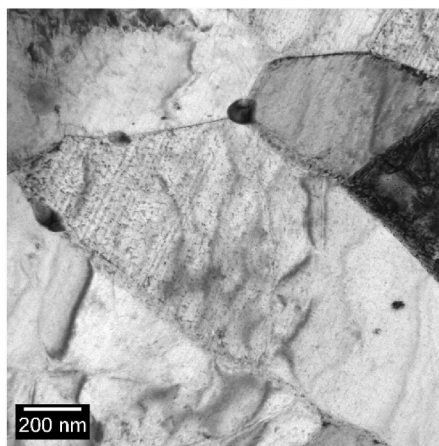conditions [62,69].

3.3.3. Evolution of precipitates

The analysis of the interrupted creep specimens shows an obvious size growth of $M_{23}C_6$ carbides. The average initial size of $M_{23}C_6$ in the as-service-exposed material is 120 nm whilst at fracture, this has increased to 250 nm, as reported in Table 5. The coarsening of $M_{23}C_6$ precipitates is followed by their coalescence as is shown in the EBSD images in Fig. 6. Precipitate coarsening is driven by the increase in the lattice/particle surface interfacial energy that happens with creep at elevated temperatures and long exposure times and follows the Ostwald ripening law [6,81]. As a consequence of coarsening and coalescence, the stabilizing effect of $M_{23}C_6$ particles on LABs is lost, facilitating
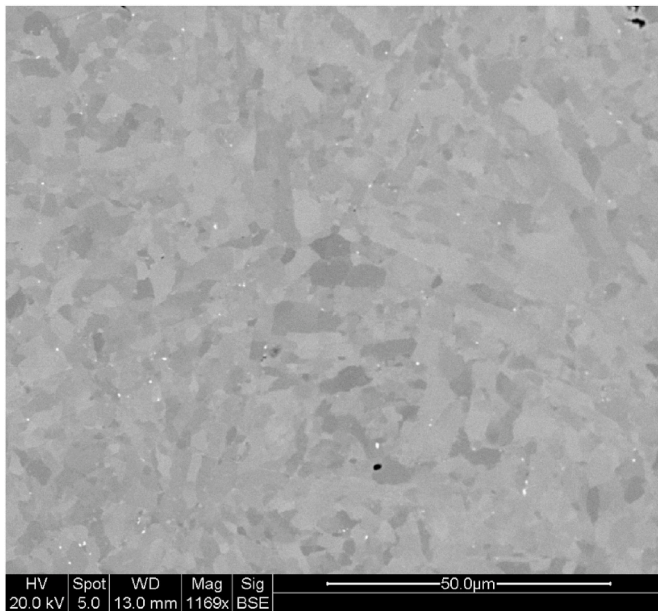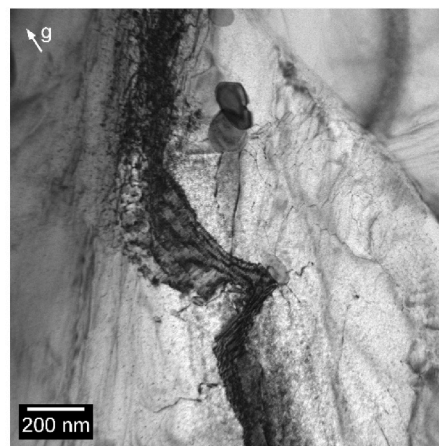
Fig. 11. SEM-BSE of P91 sample at failure (Test 4) revealing equiaxed structures and Laves phase (white spots)

knitting reactions between free dislocations and dislocations at the boundaries of laths and sub-grains, which causes the substructure to disappear [41,82,83]. Thus, the dynamic recovery is affected by the distribution and size of $M_{23}C_6$ that give the major contribution to sub-grain stabilization. As well as dynamic recovery, the transformation to an equiaxed grain structure is also influenced by the distribution and size of precipitates in the microstructure. Coarse $M_{23}C_6$ particles are present along the equiaxed grains boundaries (Fig. 12a) and it has been suggested that these particles conserve the same location as in their original martensitic lath and prior austenitic grain boundaries [77]. $M_{23}C_6$ precipitates represent a favourable position for the nucleation of the new grains due to dislocation pile-ups and tangles at the interface between precipitates and grain-boundaries that can trigger the formation of new grains (Fig. 12b) [77,84]. $M_{23}C_6$ coarsening and coalescence is one of the main creep degradation mechanisms leading to a rapid increase in the creep strain rate.

The volume fraction of MX appears to be stable during the interrupted creep tests. The stability of MX during creep helps to maintain the creep rate at minimum and contributes to keep the creep strength of the material by decreasing the microstructural instability. The distribution and presence of MX at Test 3 and 4 close to failure is shown in Fig. 10c/d [41]. In the literature, it is reported that Z-phase particles may form at the expense of MX carbonitrides [27,83], but this behaviour has not been observed in the current work under the test conditions examined. The stability of MX until about 3000 h is also demonstrated in other studies regarding the creep behaviour of 9–12% Cr steels [12,36]. Additionally, Nb/V-rich MX carbonitrides show good stability against particle coarsening during creep deformation maintaining an average size of 20 nm for NbX and 70 nm for VX [21,24].

Laves phase particles are not observed to ripen and instead maintain an approximate size of 300 nm. Thus, under the tested creep conditions, Laves phase particles show a tendency to stability against coarsening. Laves particles, for their shape and size, are preferential sites for nucleation of cavities as can be seen in Fig. 10d where a cavity is detected close to the Laves phase that grows in the proximity of a $M_{23}C_6$ particle.
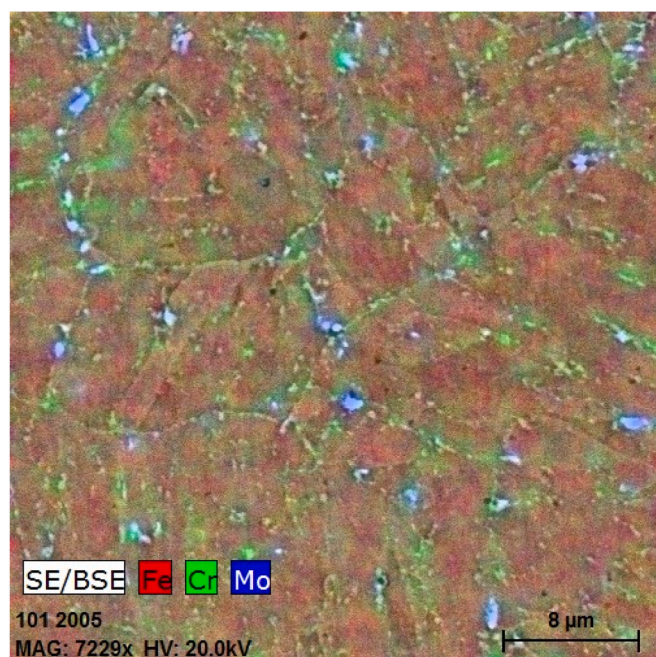
3.3.4. Creep cavities evolution

The combined effects of the processes listed above responsible for the microstructure evolution of P91 (i.e. coarsening of precipitates, Laves phase, dynamic recovery, disappearance of lath structures) cause the weakening of the material and trigger the formation of cavities [85].
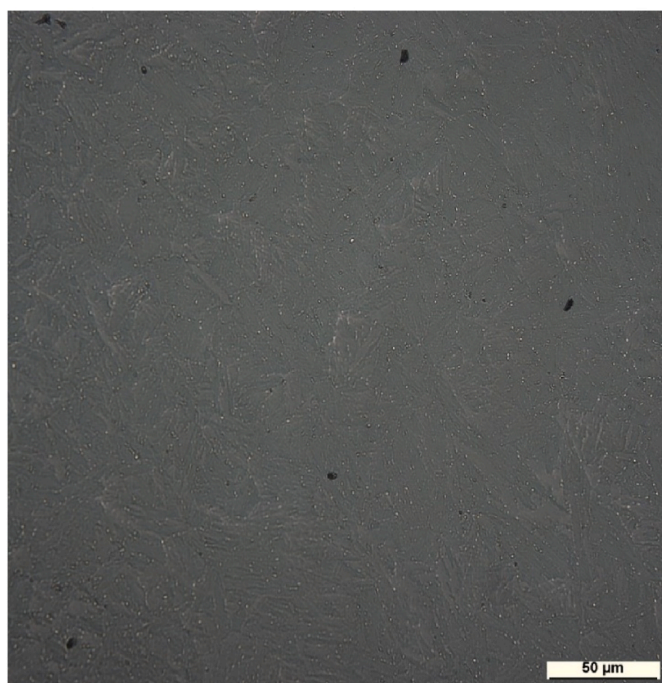
The nucleation of voids happens primarily at the interface with second phase particles such as $M_{23}C_6$ and Laves phase along grain boundaries where dislocations pile ups generating areas of high stress concentration [86–88]. The subsequent growth and coalescence of voids under creep conditions is one of the main factor for the reduction of creep strength and for creep failure [14]. Different studies have reported that cavities can nucleate both early in creep life or late in creep life depending on the microstructure and composition of the material and on the test conditions used [13,88]. For the material analysed in this paper, as reported in Table 5, pre-existing cavities are already present in the as-serviced-exposed state.

Cavities were counted using ImageJ software on microstructural images collected with an optical microscope. Cavity agglomeration and microcracks forming at the later stages of creep were not included in the cavity measurements.

Fig. 13a shows the distribution of pre-existing cavities (black holes) in the as-serviced-exposed sample that occurs mainly along PAGs in the proximity of Laves phase and $M_{23}C_6$ carbides (blue colour particles enriched in Mo and green colour particles enriched in Cr respectively) and partially along lath boundaries. Fig. 13b shows, using OM at larger scale, also the presence in the as-received material of pre-existing cavities that are quite large and circular while the white spots represent

Fig. 12. BF TEM micrographs showing (a) $M_{23}C_6$ at equiaxed grains boundaries following Test 3, and (b) pile-ups and tangles of dislocation close to precipitates following Test 2

(a)

(b)

Fig. 13. (a) EDS image showing cavity distribution in the as-service-exposed material (Cr in green indicates $M_{23}C_6$, Mo in blue Laves phase, black holes to represent cavities) (b) OM image revealing pre-existing cavities in the as-service-exposed material. (For interpretation of the references to colour in this figure legend, the reader is referred to the Web version of this article.)

precipitates. These pre-existing large cavities are thought to be pores that form for the presence of inclusions as S, Mn and Al in the composition but further investigation is needed. This finding is consistent with the study done by Yadav et al. [85] and by Siefert and Parker [13].

The evolution of cavities for creep-loaded specimens is shown in Fig. 14 for Test 2 at the onset of tertiary creep stage and for Test 4 at fracture using light optical microscope images. Fig. 14a ($t/t_r = 0.9$)

reveals some interesting features: growth of pre-existing large and circular cavities that have increased in diameter compared to the cavities in Fig. 13b, new smaller creep cavities visible around PAG boundaries forming chain-like patterns and start of coalescence. In Fig. 14b ($t/t_r = 1$), the cavities have agglomerated losing their regular and round shape, they are more elongated and micro cracks are formed.

Different modelling approaches have been evolved in the past years to describe the creep life through cavitation. A new life prediction model based on the original Hull-Rimmer creep cavity growth theory and applicable in stress controlled conditions, was developed by Jiang et al. [89] using the cavity radius as damage parameter. Even if this model claims to predict the lives in good agreement with experimental values, its application in the field is very limited since it relies on many variables that can be determined only through a deep metallographic investigation. A model able to predict the time to a given cavity area fraction was developed by Pohja et al. [90]. This model is simpler to implement in industrial applications since it uses operational variables such as time, temperature and stress as predictive variables for the creep cavitation damage but it still needs validation for long-term damage evolution. EPRI developed a model where the prediction of creep life is related to the void fraction through a parameter function of tertiary creep strain. This is the simplest method for the assessment of life in power plant components but the parameters in the model change in accordance to steel composition and microstructure and uncertainty is added from the variability of methods used for characterization [13].

Without doubt, it is possible to state that the estimation of creep life through cavitation is a hard task and reliable procedures for cavity counting and characterization of cavity damage are required.

3.4. Fracture analysis

Fractography evaluation of the failed crept sample (Test 4) by SEM reveals a mixture of transgranular ductile dimple and intergranular fracture modes that is typical for short-term creep testing at high plastic deformation [6,46,91]. The creep crack nucleates on the outer rim due to necking that is caused by the accumulation of plastic strain. Dimples contain inclusions and second-phase particles that have been identified by EDS as MnS and M23C6 (Fig. 15a and b). These are preferred sites for microvoid nucleation being locations of stress concentrations. Voids nucleate, grow and, after a certain threshold is exceeded, coalesce under the effect of plastic deformation. At the stress level of 80 MPa, just a few microcracks are formed since cracks give the strongest contribution to creep failure at higher stress [14]. Void coalescence is therefore the main reason for creep damage. Cavities have been found to form also around Laves phase (see Fig. 6 at $t/t_r = 1$). Laves phase particles, with their broad and irregular dimensions and their brittleness, have been found to be areas of strain concentration that enhance the nucleation of voids and therefore the deterioration of creep strength [19] possibly triggering the transition from ductile to brittle fracture mode [42].

3.5. Softening mechanism

Creep models that relate the creep response to the evolution of microstructural parameters have already been successfully developed. Xiao et al. [92] modelled the creep deformation of a G115 steel (a tempered martensitic steel) through a modified version of Orowan's equation where the softening effect caused by precipitation coarsening and creep cavitation was incorporated via two damage parameters. Yadav et al. [74] developed a model for P91 steel based on a hybrid concept where a physical-based approach, used to describe the microstructural evolution, is coupled with the continuum damage mechanics (CDM) theory used to address damage evolution. These models exhibit a good agreement with the experimental creep data at various creep conditions but their application in the power generation industry is not widespread since they are based on the time-intensive detailed
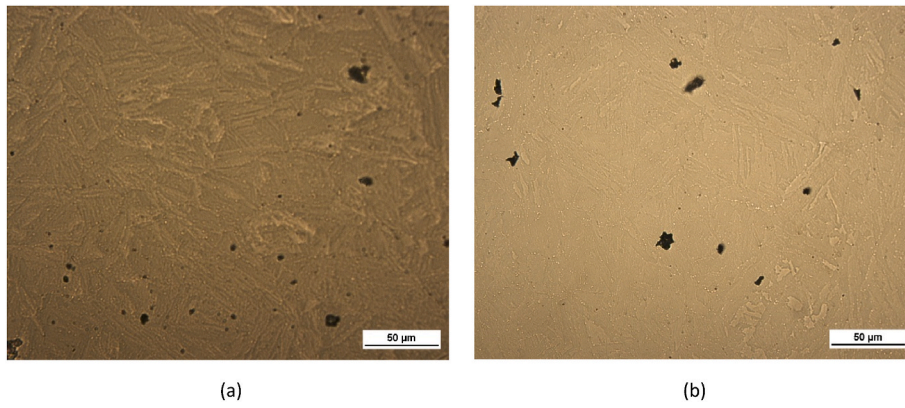
Fig. 14. OM images of (a) cavities at Test 2 ($t/t_r = 0.9$) and (b) cavities and micro cracks at fracture
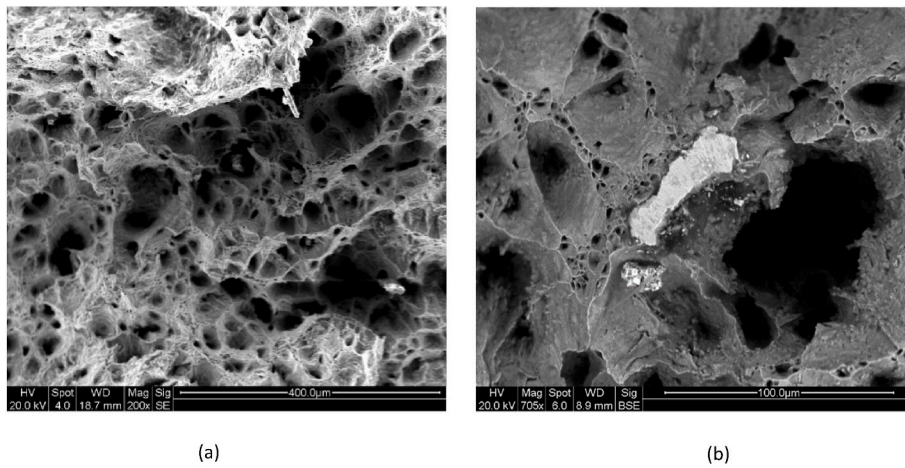

Fig. 15. SEM images of fracture surfaces following Test 4, (a) SE showing dimples with some containing inclusions, and (b) BSE showing detail of MnS inclusion (bright area)

measurement of a variety of microstructural parameters such as for example dislocation densities, sub-grain size, number of precipitates per unit volume and precipitate mean radii.

Hardness instead is a measurable indicator of the microstructural softening that happens under creep exposure due to the internal material mechanisms listed in section 3.3, i.e. lath widening and substructure disappearance, particle coarsening and coalescence, recovery and formation of equiaxed grains [93]. Hardness has been used to develop models for the remaining life of high temperature components often in relation with the Larson-Miller parameter (LMP) [32]. Fig. 16 shows the evolution of hardness measured at room temperature (RT) with life fraction.
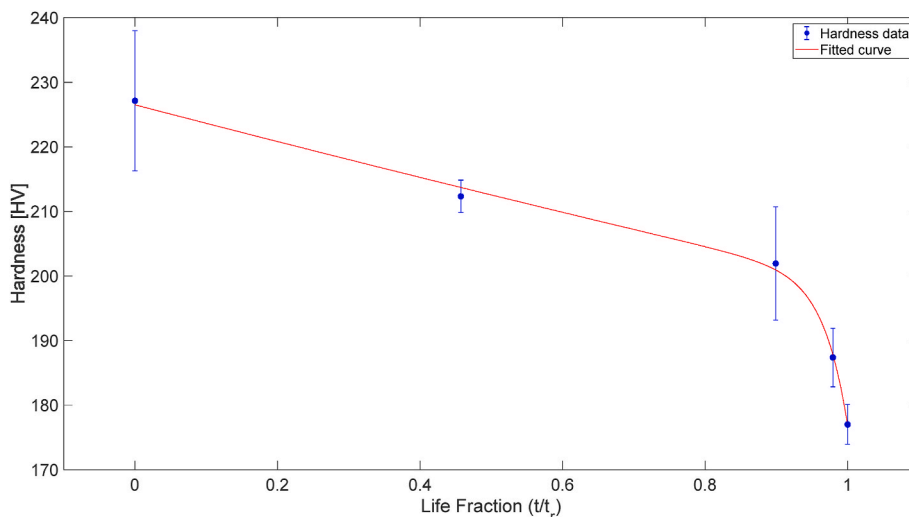

Fig. 16. Hardness evolution of the service-exposed P91 as a function of creep life fraction

The mean value of hardness for the as-service-exposed P91 is 227 HV whilst following creep rupture, it has dropped to 177 HV. The best relation that represents the evolution of hardness as function of life fraction at RT is given by a two terms exponential equation given in Equation (3), for which goodness of fit can be seen in Fig. 16.

$$HV = -2.07 \times 10^{-12} \exp\left(30\frac{t}{t_r}\right) + 226.5 \exp\left(-0.127\frac{t}{t_r}\right) \qquad (3)$$

Following the work done by Masuyama [11,94], a linear empirical equation between hardness ratio and life fraction can be extrapolated once the hardness ratio is calculated from the original hardness value for the as-service-exposed sample HV_0.

$$\frac{HV}{HV_0} = -0.186\frac{t}{t_r} + 1.01 \qquad (4)$$

Equation (4) is very similar to the one proposed by Masuyama [11, 94]. The advantage of Equation (3) is the ability to describe accurately the acceleration of hardness drop in the tertiary creep stage.

The hardness variation is faster from $t/t_r = 0.9$ at the onset of tertiary creep while until the secondary creep stage the hardness reduction is less rapid and it is characterised by a more linear behaviour. The significant change in the slope of hardness curve at $t/t_r = 0.9$ could be an indication of a change in the controlling mechanism for creep deformation. This would confirm the outcomes research in the literature [93].

Previous research reports a hardness evolution shape as above and attributes the main reason for hardness decline to the widening of the lath structure during long-term creep [11] and to particle coarsening during short-term creep [38,39,95]. On the other hand, the increase in lath size is closely related to changes in precipitation behaviour and to a change in the interaction between precipitates and dislocations. Dislocation rearrangement is known to be the dominant creep deformation mechanism for high-strength martensitic steel [92].

Hardness is known to be proportional to the square root of dislocation density through the relation between hardness and the flow stress, and therefore hardness is indirectly related as well to subgrain size and precipitates [11]. The effect on hardness from lath strengthening is estimated by the Hall-Petch relationship where the grain growth is accounted for by introducing an evolution equation for the grain
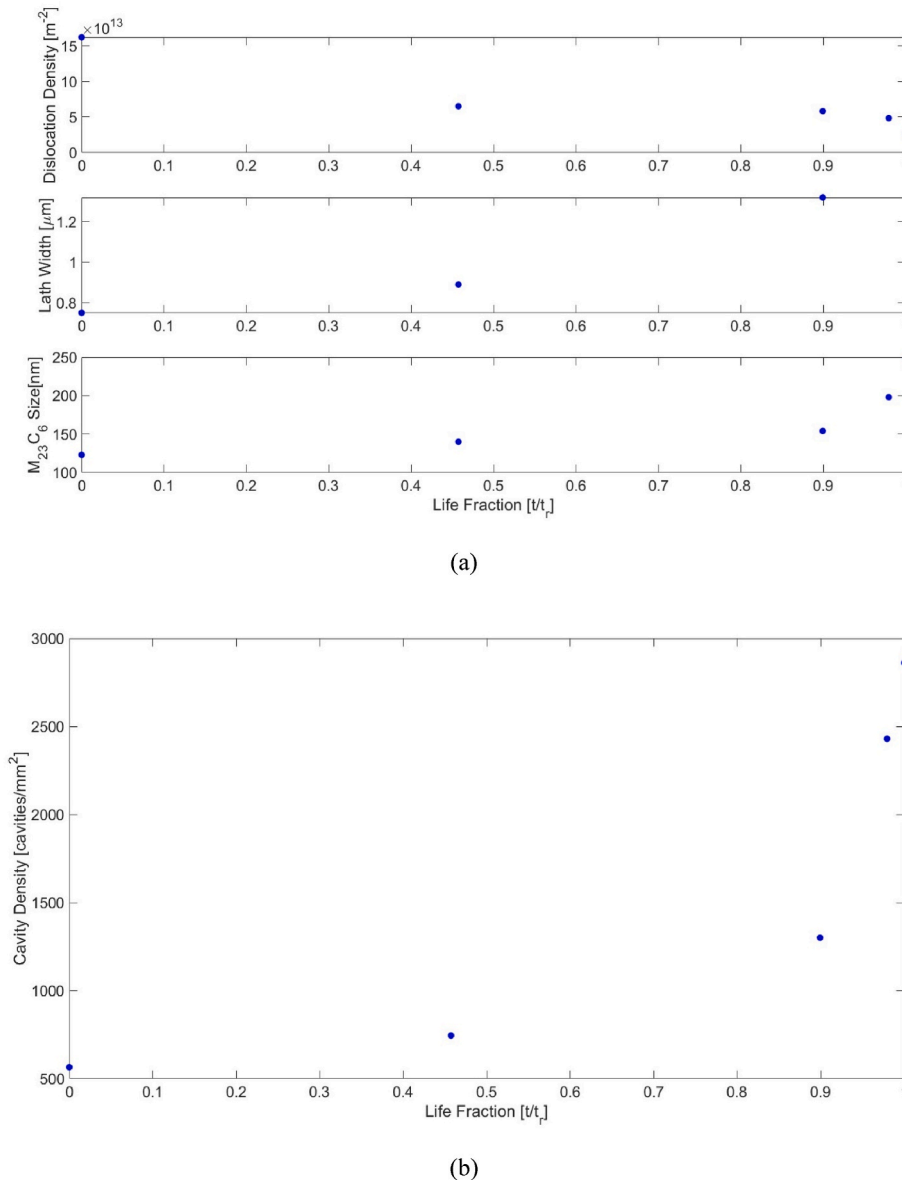

(a)

(b)

Fig. 17. Evolution of microstructural features in service-exposed P91 as a function of creep: (a) evolution of microstructural parameters, (b) evolution of cavity density

diameter. The relationship between hardness and precipitation strengthening is established by the Orowan's law that is coupled with the Ostwald ripening process equation to describe precipitation coarsening [32,96].

The growth and disappearance of subgrains and lath structure, the decrease of dislocation density, the coarsening of precipitates during creep and the presence of Laves phase cause hardness to decline. Apart from these microstructural changes, also the increase in creep cavity density plays a key role in the fall of hardness (see paragraph 3.3.4).

What is challenging in creep strength-enhanced ferritic steel (9–12% Cr) is the understanding of the importance and the influence of each microstructural process on the creep behaviour of the steel [97]. Microstructural degradation and creep cavitation normally occur at the same time but the predominance of each factor is different according the original microstructure, creep conditions and stress state [96]. Fig. 17 shows the evolution of the main factors throughout the creep life with the values taken from Table 5.

From Fig. 17 it appears that microstructural changes are most influential during the secondary creep stage whilst cavity evolution is more significant in the tertiary creep stage where the cavitation rate is higher. At the onset of tertiary stage, the coarsening of $M_{23}C_6$ (associated with decrease in number of dislocations and increase in interparticle spacing) can trigger a faster nucleation and growth of cavities that finally lead to material failure. This would support the assertions made by the authors in the paper for CrMoV [93] but further data need to be collected from laboratory tests to assess the importance of individual microstructural factors and to develop more insightful predictive models for creep life. Also, creep cavities results in the tertiary creep behaviour [92,98].

Nonetheless, it is possible to state that all the aforementioned processes are responsible for creep damage and contribute to the decrease of hardness so that hardness measurement can be used as method to estimate the material microstructural creep degradation and to develop predictive lifing models [67,93].

A hardness-based model for rupture life estimation has been proposed by the authors in Ref. [93] for CrMoV steel. Since the physical basis of the model is similar to the findings in the present study, the validity of the model could be extended also to P91 steel and in general to all high-strength martensitic steels (because of their very similar microstructure) using material-specific parameters. Finally, the validation of the model should be performed with measured and existing values from creep tests or inspection data.

4. Conclusion

The degradation of the microstructure for a P91 steel and its effect on the material mechanical properties has been investigated through interrupted creep tests and the results have been discussed in this paper. A good understanding of the microstructure evolution for 9–12% Cr steels is extremely important in order to evaluate their reliability during service under high temperature and stress conditions. The main factors affecting the increase in the creep rate and the reduction in hardness are summarized as follows: i) decrease of mobile free dislocations inside the lath structure by dynamic recovery processes, ii) disappearance of martensitic lath structure and final transformation into an equiaxed microstructure, iii) coarsening/coalescence of $M_{23}C_6$ precipitates and broad Laves phase both providing nucleation sites for cavities, iv) creep cavitation.

During the secondary creep stage, the lath and sub-grain structure and the fine distribution of precipitates counterbalance the start of the dynamic recovery process with the effect of keeping the creep rate stable and with a slight hardness reduction. From the tertiary creep stage the internal material changes listed above from i) to iii) are more rapid and together with the significant increase of cavity density, the creep rate accelerates until the final fracture and the hardness rapidly drops. Fig. 18 provides a schematic summary of the internal mechanisms that influence the change in the creep strain curve.

Further to Fig. 18, it is possible to develop an "interactive diagram" shown in Fig. 19 to illustrate the interactions between the various microstructural and mechanical variables, which collectively contribute to the degradation of the material (deformation mechanisms) and eventually lead to creep rupture.

The changes in the microstructure lead to a complex interaction between primary microstructural features such as dislocations, precipitates, lattice and cavities. The understanding of their relationship is facilitated through the microstructural characterization of the material by microscopy techniques as TEM and SEM and diffraction techniques as EBSD. Industrial practice uses periodic inspections, mainly non-destructive techniques, such as hardness measurement because of their ease of implementation and cost effectiveness. Thus, a hardness-based model would complement current inspection practice and should be further developed for the prediction of creep life. Hardness can be successfully deployed as indicator for the estimation of creep damage since it has been seen from Section 3.5 that Vickers hardness changes can be related to the variation of dislocation, $M_{23}C_6$, lath structure and voids.
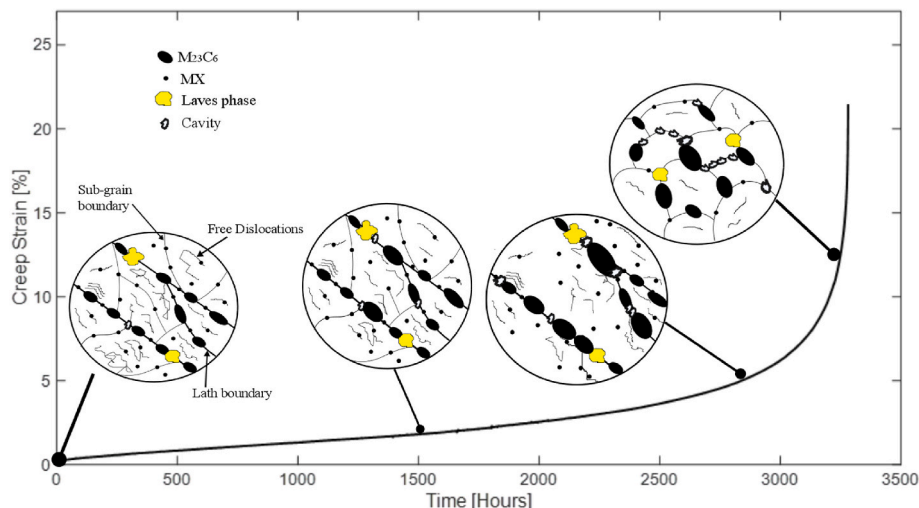
Hardness-based models would be welcomed for practical

Fig. 18. Schematic representation of microstructure changes during creep
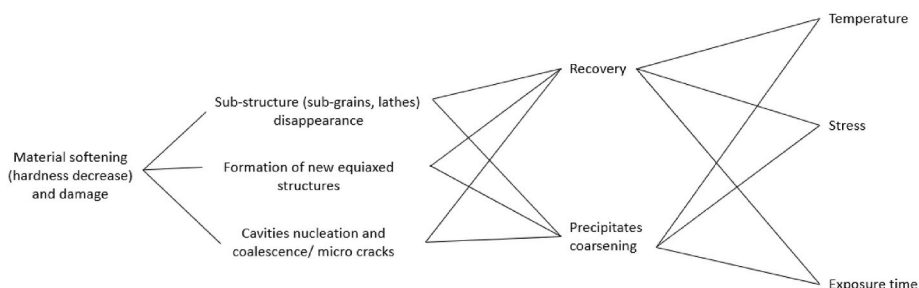
Fig. 19. Interactive diagram illustrating the relationship between microstructural changes and final damage. Input: Temperature, stress and exposure time. Output: Material softening and final damage

deployment to support decisions on operating plant. However, there are some important requirements to ensure reliable deployment of the model on operating plant.

1. The Station should adopt a consistent approach to the collection of inspection data over successive outages, and operational data, to provide the information required to optimise the model.
2. The authors have developed similar models for CrMoV steels in use on high temperature plant based on field inspection data resulting from very long exposure times to plant operating conditions [93]. This CrMoV model showed a transition in behaviour when cavitation was seen to dominate the later stages of useable life. Importantly this showed the benefits of implementing a systematic inspection schedule.
3. Hence, the use of a similar P91 model in the field could be calibrated and optimised to account for plant operating conditions, which can be achieved if point 1 above is adopted in conjunction with suitable laboratory tests.

The insights given in this paper aimed to give an exhaustive explanation of the main microstructural factors involved in the structural stability of P91 during service and how these factors have an impact on the softening of the material. Further research is needed to focus on the improvement of life assessment techniques for long-term creep exposure. New models should investigate the impact of each microstructural parameter on the variation of hardness so that hardness-based life techniques incorporating service conditions can be used in conjunction with other monitoring strategies as non-destructive examination in order to assist in determining the safe operating life for the material under investigation.

Data availability statement

The raw/processed data required to reproduce these findings cannot be shared at this time as the data also forms part of an ongoing study.

Declaration of competing interest

The authors declare that they have no known competing financial interests or personal relationships that could have appeared to influence the work reported in this paper.

Acknowledgments

References

[1] Gibon T, Arvesen A, Hertwich EG. Life cycle assessment demonstrates environmental co-benefits and trade-offs of low-carbon electricity supply options. Renew Sustain Energy Rev 2017/09/01, 2017;76:1283–90.

[2] Bass RJ, Malalasekera W, Willmot P, Versteeg HK. The impact of variable demand upon the performance of a combined cycle gas turbine (CCGT) power plant. Energy 2011/04/01, 2011;36(4):1956–65.

[3] Ibrahim Tk, Mohammed MK, Awad OI, Rahman MM, Najafi G, Basrawi F, Abd Alla AN, Mamat R. The optimum performance of the combined cycle power plant: a comprehensive review. Renew Sustain Energy Rev 2017/11/01, 2017;79:459–74.

[4] Ramachandra T. Renewable energy transition: perspective and challenges. Energy India 2020:175–83.

[5] Gielen D, Boshell F, Saygin D, Bazilian MD, Wagner N, Gorini R. The role of renewable energy in the global energy transformation. Energy Strategy Rev 2019/04/01, 2019;24:38–50.

[6] Sklenička V, Kuchařová K, Král P, Kvapilová M, Svobodová M, Čmakal J. The effect of hot bending and thermal ageing on creep and microstructure evolution in thick-walled P92 steel pipe. Mater Sci Eng, A 2015;644:297–309.

[7] Tillman DA. Chapter eight - coal-fired power plants: 2000–present and beyond. In: Tillman DA, editor. Coal-fired electricity and emissions control. Butterworth-Heinemann; 2018. p. 207–36.

[8] Nomoto H. 24 - advanced ultrasupercritical pressure steam turbines and their combination with carbon capture and storage systems. In: Tanuma T, editor. Advances in steam turbines for modern power plants. second ed.). Woodhead Publishing; 2022. p. 601–19.

[9] 2 - rankine cycle and variants. In: Markides CN, Wang K, editors. Power generation technologies for low-temperature and distributed heat. Woodhead Publishing; 2023. p. 49–161.

[10] Wang Y, Zhang W, Wang Y, Feng Z. Characteristics of premature creep failure in over-tempered base metal of grade 91 steel weldment. Int J Pres Ves Pip 2021;192: 104396.

[11] Masuyama F. Hardness model for creep-life assessment of high-strength martensitic steels. Mater Sci Eng, A 2009;510:154–7.

[12] Sklenička V, Kuchařová K, Svoboda M, Kloc L, Buršík J, Kroupa A. Long-term creep behavior of 9–12% Cr power plant steels. Mater Char 2003;51(1):35–48.

[13] Siefert JA, Parker JD. Evaluation of the creep cavitation behavior in Grade 91 steels. Int J Pres Ves Pip 2016;138:31–44.

[14] Han K, Ding H, Fan X, Li W, Lv Y, Feng Y. Study of the creep cavitation behavior of P91 steel under different stress states and its effect on high-temperature creep properties. J Mater Res Technol 2022;20:47–59.

[15] Samantaray D, Phaniraj C, Mandal S, Bhaduri A. Strain dependent rate equation to predict elevated temperature flow behavior of modified 9Cr-1Mo (P91) steel. Mater Sci Eng, A 2011;528(3):1071–7.

[16] Parker J, Henry J. The performance of creep-strengthened ferritic steels in power generating plant. In: ASME 2007 pressure vessels and piping conference; 2007. p. 607–16.

[17] Siefert J, Parker J. Evaluation of the creep cavitation behavior in Grade 91 steels. Int J Pres Ves Pip 2016;138:31–44.

[18] Pandey C, Giri A, Mahapatra M. Evolution of phases in P91 steel in various heat treatment conditions and their effect on microstructure stability and mechanical properties. Mater Sci Eng, A 2016;664:58–74.

[19] Xu Y, Nie Y, Wang M, Li W, Jin X. The effect of microstructure evolution on the mechanical properties of martensite ferritic steel during long-term aging. Acta Mater 2017;131:110–22.

[20] Zhao H, Wang Z, Han X, Wang M. Effect of long-term aging on the microstructural evolution in a P91 steel. Materials 2022;15(8):2847.

[21] Sawada K, Kubo K, Abe F. Creep behavior and stability of MX precipitates at high temperature in 9Cr–0.5Mo–1.8W–VNb steel. Mater Sci Eng, A 2001;319–321: 784–7.

[22] Mitsuhara M, Yamasaki S, Miake M, Nakashima H, Nishida M, Kusumoto J, Kanaya A. Creep strengthening by lath boundaries in 9Cr ferritic heat-resistant steel. Phil Mag Lett 2016;96(2):76–83.

[23] Panait C, Zielińska-Lipiec A, Kozieł T, Czyrska-Filemonowicz A, Gourgues-Lorenzon A-F, Bendick W. Evolution of dislocation density, size of subgrains and MX-type precipitates in a P91 steel during creep and during thermal ageing at 600 °C for more than 100,000 h. Mater Sci Eng 2010;527.

[24] Dudko V, Belyakov A, Molodov D, Kaibyshev R. Microstructure evolution and pinning of boundaries by precipitates in a 9 pct Cr heat resistant steel during creep. Metall Mater Trans 2013;44(1):162–72.

[25] Hongo H, Tabuchi M, Watanabe T. Type IV creep damage behavior in Gr.91 steel welded joints. Metall Mater Trans 2012;43(4):1163–73.

[26] Erten DT, Nguyen TT, Jeong TM, Yoon KB. Creep deformation and rupture behaviour of service exposed P91 weld and base steel measured by miniature tensile creep testing. Mater A T High Temp 2017;34(5–6):425–33.

[27] Danielsen HK, Hald J. Behaviour of Z phase in 9–12% Cr steels. Energy Materials 2006;1(1):49–57.

[28] Maharaj C, Dear J, Morris A. A review of methods to estimate creep damage in low-alloy steel power station steam pipes. Strain 2009;45(4):316–31.

[29] Sposito G, Ward C, Cawley P, Nagy P, Scruby C. A review of non-destructive techniques for the detection of creep damage in power plant steels. NDT E Int 2010;43(7):555–67.

[30] Zhu L, Liu X, Fan P, Yang Y, Zhang K, Wang K, Wang L. Evaluation of microstructure degradation during creep of P91 steel using electrochemical detection technique. Mater Today Commun 2023;34:105039.

[31] Allen DJ, Fenton ST. A hardness-based creep rupture model for new and service aged P91 steel. 2007.

[32] Mukhopadhyay S, Roy H, Roy A. Development of hardness-based model for remaining life assessment of thermally loaded components. Int J Pres Ves Pip 2009;86(4):246–51.

[33] Bonetti R, Morris A, Shipway PH, Sun W. Empirical relationships between hardness, replica and strain and their roles in health monitoring based life assessment for aged power plant materials. Int J Pres Ves Pip 2022;199:104735.

[34] Guguloth K, Roy N. Creep deformation behavior of 9Cr1MoVNb (ASME Grade 91) steel. Mater Sci Eng, A 2017;680:388–404.

[35] Pohja R, Tuurna S, Hakala TJ, Auerkari P, McNiven U, Laaksonen L, Nikkarila R. Life assessment and maintenance of welded piping operating at high temperatures. In: Baltica IV-Energiantuotannon kunnossapitokokemukset; 2019.

[36] Ghassemi Armaki H, Chen R, Maruyama K, Igarashi M. Creep behavior and degradation of subgrain structures pinned by nanoscale precipitates in strength-enhanced 5 to 12 pct Cr ferritic steels. Metall Mater Trans 2011;42:3084–94.

[37] Panait CG, Bendick W, Fuchsmann A, Gourgues-Lorenzon AF, Besson J. Study of the microstructure of the Grade 91 steel after more than 100,000 h of creep exposure at 600 °C. Int J Pres Ves Pip 2010;87(6):326–35.

[38] Aghajani A, Somsen C, Eggeler G. On the effect of long-term creep on the microstructure of a 12% chromium tempered martensite ferritic steel. Acta Mater 2009;57(17):5093–106. 2009/10/01/.

[39] Zhu L, Liu X, Fan P, Liu J. A study of microstructure evolution during creep of 9Cr-1Mo steel using ultrasonic and hardness measurements. J Mater Eng Perform 2019;28:2348–55.

[40] Zhang K, Liu X, Zhu L. Characterisation of microstructure evolution during creep of P91 steel using the electron backscatter diffraction technique. Mater A T High Temp 2021;38(3):158–65.

[41] Cerri E, Evangelista E, Spigarelli S, Bianchi P. Evolution of microstructure in a modified 9Cr–1Mo steel during short term creep. Mater Sci Eng, A 1998;245(2):285–92.

[42] Yan W, Wang W, Shan YY, Yang K. Microstructural stability of 9–12%Cr ferrite/martensite heat-resistant steels. Front Mater Sci 2013;7(1):1–27.

[43] Lekakh SN, Buchely M, Li M, Godlewski L. Effect of Cr and Ni concentrations on resilience of cast Nb-alloyed heat resistant austenitic steels at extreme high temperatures. Mater Sci Eng, A 2023;873:145027.

[44] Liu T, Cui Y, Zheng K, Yin F, Luo Z. Synergistic effect of grain size and second-phase particle on the oxidation behaviour of a high-manganese austenitic heat-resistant steel. Corrosion Sci 2023;215:111054.

[45] Parker J, Siefert J. Metallurgical and stress state factors which affect the creep and fracture behavior of 9% Cr steels. Adv Mater Sci Eng 2018;2018:1–15.

[46] Benaarbia A, Xu X, Sun W, Becker AA, Jepson MAE. Investigation of short-term creep deformation mechanisms in MarBN steel at elevated temperatures. Mater Sci Eng, A 2018/09/12/, 2018;734:491–505.

[47] J Appl Phys vol. 42, pp. 4290-4295.".

[48] Yakel H. Atom distributions in tau-carbide phases: Fe and Cr distributions in (Cr23− xFex) C6 with x= 0, 0· 74, 1· 70, 4· 13 and 7· 36. Acta Crystallogr, Sect B: Struct Sci 1987;43(3):230–8.

[49] Gladyshevskii E, Kuz'ma YB. Crystal structure of ternary phases in the systems Mo (W)-Fe (Co, Ni)-Si. J Struct Chem 1960;1(1):57–62.

[50] Kim SJ, Franzen H, Lengauer W. Non-stoichiometry and twinning in NbN1− x: a study of synthesis and structure in a defect NaCl-type solid. Journal of the Less Common Metals 1990;160(1):193–6.

[51] Sonderegger B, Mitsche S, Cerjak H. Microstructural analysis on a creep resistant martensitic 9–12% Cr steel using the EBSD method. Mater Sci Eng, A 2008;481–482:466–70.

[52] Hyde TH, Sun W, Becker AA, Williams JA. Creep properties and failure assessment of new and fully repaired P91 pipe welds at 923 K. Proc Inst Mech Eng Part L 2004;218(3):211–22.

[53] S. G. GMBH. "1.4903 (X10CRMOVNB9-1) Quenched and Tempered "; https://www.stahlportal.com/en/stock/14903-x10crmovnb9-1-quenched-and-tempered/.

[54] Zhang J, Li J, Zan J, Guo Z, Liu K. A creep constitutive model, based on deformation mechanisms and its application to creep crack growth. Metals 2022;12:2179.

[55] Dieter GE, Bacon D. Mechanical metallurgy. New York: McGraw-hill; 1976.

[56] Yadav SD, Kalácska S, Dománková M, Yubero DC, Resel R, Groma I, Beal C, Sonderegger B, Sommitsch C, Poletti C. Evolution of the substructure of a novel 12% Cr steel under creep conditions. Mater Char 2016;115:23–31.

[57] Po G, Huang Y, Li Y, Baker K, Flores BR, Black T, Hollenbeck J, Ghoniem N. A model of thermal creep and annealing in finite domains based on coupled dislocation climb and vacancy diffusion. J Mech Phys Solid 2022;169:105066.

[58] Fournier B, Sauzay M, Pineau A. Micromechanical model of the high temperature cyclic behavior of 9–12%Cr martensitic steels. Int J Plast 2011;27(11):1803–16.

[59] Sawada K, Maruyama K, Hasegawa Y, Muraki T. Creep life assessment of high chromium ferritic steels by recovery of martensitic lath structure. Key Eng Mater 1999;171–174:109–14.

[60] Ryde L. Application of EBSD to analysis of microstructures in commercial steels. Mater Sci Technol 2006;22:1297–306.

[61] Collomb S, Gressel P, Ghanbaja J, Jacques A, Redjaïmia A. Characterization of welded joint in martensitic steel Grade 91 after interrupted creep test at 600 °C. Mater Sci Eng, A 2022;855:143851.

[62] Zhao J, Gong J, Saboo A, Dunand DC, Olson GB. Dislocation-based modeling of long-term creep behaviors of Grade 91 steels. Acta Mater 2018;149:19–28.

[63] Ghoniem NM, Matthews J, Amodeo RJ. A dislocation model for creep in engineering materials. Res Mech 1990;29(3):197–219.

[64] Schäfer C, Mohles V, Gottstein G. Modeling of non-isothermal annealing: interaction of recrystallization, recovery, and precipitation. Acta Mater 2011;59 (17):6574–87.

[65] Guo Z, Ma T, Yang X, Li W, Xu Q, Li Y, Li J, Vairis A. Comprehensive investigation on linear friction welding a dissimilar material joint between Ti17(α+β) and Ti17 (β): microstructure evolution, failure mechanisms, with simultaneous optimization of tensile and fatigue properties. Mater Sci Eng, A 2024/09/01/, 2024;909:146818.

[66] Norfleet DM, Dimiduk DM, Polasik SJ, Uchic M, Mills MJ. Dislocation structures and their relationship to strength in deformed nickel microcrystals. Acta Mater 2008;56(13):2988–3001.

[67] Abe F, Kern T-U, Viswanathan R. Creep-resistant steels. Elsevier; 2008.

[68] Pandey C, Mahapatra M, Kumar P, Vidyarthy R, Srivastava A. Microstructure-based assessment of creep rupture behaviour of cast-forged P91 steel. Mater Sci Eng, A 2017;695:291–301.

[69] Pešička J, Kužel R, Dronhofer A, Eggeler G. The evolution of dislocation density during heat treatment and creep of tempered martensite ferritic steels. Acta Mater 2003;51(16):4847–62.

[70] Tang B, Jiang L, Hu R, Li Q. Correlation between grain boundary misorientation and M23C6 precipitation behaviors in a wrought Ni-based superalloy. Mater Char 2013;78:144–50.

[71] Hong HU, Rho BS, Nam SW. Correlation of the M23C6 precipitation morphology with grain boundary characteristics in austenitic stainless steel. Mater Sci Eng, A 2001;318(1):285–92.

[72] Park JK, Ardell AJ. Precipitation at grain boundaries in the commercial alloy Al 7075. Acta Metall 1986;34(12):2399–409.

[73] Priester L. Precipitation at grain boundaries. In: Grain boundaries: from theory to engineering, vol. 7. Dordrecht: Springer; 2012. p. 217–40.

[74] Yadav S, Scherer T, Reddy GP, Laha K, Sasikala G, Albert S, Poletti C. Creep modelling of P91 steel employing a microstructural based hybrid concept. Eng Fract Mech 2018;200:104–14.

[75] Isik M, Kostka A, Eggeler G. On the nucleation of Laves phase particles during high-temperature exposure and creep of tempered martensite ferritic steels. Acta Mater 2014;81:230–40.

[76] Derazkola HA, García Gil E, Murillo-Marrodán A, Méresse D. Review on dynamic recrystallization of martensitic stainless steels during hot deformation: Part I—experimental Study. Metals 2021;11(4):3–25.

[77] Gao Q, Di X, Liu Y, Yan Z. Recovery and recrystallization in modified 9Cr-1Mo steel weldments after post-weld heat treatment. Int J Pres Ves Pip 2012;93:69–74.

[78] Sauzay M. Modelling of the evolution of micro-grain misorientations during creep of tempered martensite ferritic steels. Mater Sci Eng, A 2009;510–511:74–80.

[79] Barrett RA, O'Donoghue PE, Leen SB. A physically-based constitutive model for high temperature microstructural degradation under cyclic deformation. Int J Fatig 2017;100:388–406.

[80] Giroux PF, Dalle F, Sauzay M, Malaplate J, Fournier B, Gourgues-Lorenzon AF. Mechanical and microstructural stability of P92 steel under uniaxial tension at high temperature. Mater Sci Eng, A 2010;527(16–17):3984–93.

[81] Hald J. Microstructure and long-term creep properties of 9–12% Cr steels. Int J Pres Ves Pip 2008;85(1):30–7.

[82] Eggeler G. The effect of long-term creep on particle coarsening in tempered martensite ferritic steels. Acta Metall 1989;37(12):3225–34.

[83] Kaibyshev R, Mishnev R, Fedoseeva A, Dudova N. The role of microstructure in creep strength of 9-12%Cr steels. Mater Sci Forum 2017;879:36–41.

[84] Dasari S, Sarkar A, Sharma A, Gwalani B, Choudhuri D, Soni V, Manda S, Samajdar I, Banerjee R. Recovery of cold-worked Al0. 3CoCrFeNi complex concentrated alloy through twinning assisted B2 precipitation. Acta Mater 2021;202:448–62.

[85] Yadav SD, Sonderegger B, Sartory B, Sommitsch C, Poletti C. Characterisation and quantification of cavities in 9Cr martensitic steel for power plants. Mater Sci Technol 2015;31(5):554–64.

[86] Yoo M, Trinkaus H. Crack and cavity nucleation at interfaces during creep. Metall Trans A 1983;14:547–61.

[87] Kassner M, Hayes T. Creep cavitation in metals. Int J Plast 2003;19(10):1715–48.

[88] Yadav SD, Jäntsch U, Scherer T, Ahmadi MR, Rosc J, Poletti C. Investigation of creep cavities in a novel 12Cr0.36Ta steel employing three-dimensional electron backscatter diffraction technique. Mater Lett 2017;207:76–9.

[89] Jiang H, Chen X, Fan Z, Dong J, Lu S. A new empirical life prediction method for stress controlled fatigue–creep interaction. Mater Lett 2008;62(24):3951–3.

[90] Pohja R, Auerkari P, Vilaça P. Modelling for creep cavitation damage and life of three metallic materials. Mater A T High Temp 2022;39(1):86–96.

[91] Eggeler G, Earthman J, Nilsvang N, Ilschner B. Microstructural study of creep rupture in a 12% chromium ferritic steel. Acta Metall 1989;37(1):49–60.

[92] Xiao B, Yadav SD, Zhao L, Tang Z, Han Y, Yang X, Kai J-J, Yang T, Xu L. Deep insights on the creep behavior and mechanism of a novel G115 steel: micromechanical modeling and experimental validation. Int J Plast 2021;147: 1–15. 103124.

[93] Bonetti R, Morris A, Shipway P, Sun W. Empirical relationships between hardness, replica and strain and their roles in health monitoring based life assessment for aged power plant materials. Int J Pres Ves Pip 2022;199:104735.

[94] Masuyama F. Advances in creep damage/life assessment technology for creep strength enhanced ferritic steels. Procedia Eng 2013;55:591–8.

[95] Sawada K, Maruyama K, Hasegawa Y, Muraki T. Creep life assessment of high chromium ferritic steels by recovery of martensitic lath structure. Key Eng Mater 1999;171:109–14.

[96] Cane B, Aplin P, Brear J. A mechanistic approach to remanent creep life assessment of low alloy ferritic components based on hardness measurements. 1985.

[97] J. Parker, "Creep cavitation in CSEF steels." p. 714.

[98] Xiao B, Xu L, Tang Z, Zhao L, Jing H, Han Y, Li H. A physical-based yield strength model for the microstructural degradation of G115 steel during long-term creep. Mater Sci Eng, A 2019;747:161–76.